

University of Texas Rio Grande Valley

ScholarWorks @ UTRGV

---

Earth, Environmental, and Marine Sciences  
Faculty Publications and Presentations

College of Sciences

---

4-2020

## The Simulated Biological Response to Southern Ocean Eddies via Biological Rate Modification and Physical Transport

Tyler Rohr

Cheryl S. Harrison  
*The University of Texas Rio Grande Valley*

Matthew C. Long

Peter Gaube

Scott C. Doney

Follow this and additional works at: [https://scholarworks.utrgv.edu/eems\\_fac](https://scholarworks.utrgv.edu/eems_fac)



Part of the [Earth Sciences Commons](#), [Environmental Sciences Commons](#), and the [Marine Biology Commons](#)

---

### Recommended Citation

Rohr, T., Harrison, C., Long, M. C., Gaube, P., & Doney, S. C. (2020). The simulated biological response to Southern Ocean eddies via biological rate modification and physical transport. *Global Biogeochemical Cycles*, 34, e2019GB006385. <https://doi.org/10.1029/2019GB006385>

This Article is brought to you for free and open access by the College of Sciences at ScholarWorks @ UTRGV. It has been accepted for inclusion in Earth, Environmental, and Marine Sciences Faculty Publications and Presentations by an authorized administrator of ScholarWorks @ UTRGV. For more information, please contact [justin.white@utrgv.edu](mailto:justin.white@utrgv.edu), [william.flores01@utrgv.edu](mailto:william.flores01@utrgv.edu).



# Global Biogeochemical Cycles

## RESEARCH ARTICLE

10.1029/2019GB006385

### Key Points:

- Net phytoplankton population growth rates are generally reduced in cyclones and inflated in anticyclones
- Anomalous biomass is highly variable, but cyclones and anticyclones rarely modify biomass in the same direction at the same time and place
- In South Pacific ACC eddies, the largest biomass anomalies are driven by biological mechanisms but switch direction from winter to spring

### Supporting Information:

- Supporting Information S1

### Correspondence to:

T. Rohr,  
trohr@mit.edu

### Citation:

Rohr, T., Harrison, C., Long, M. C., Gaube, P., & Doney, S. C. (2020). The simulated biological response to Southern Ocean eddies via biological rate modification and physical transport. *Global Biogeochemical Cycles*, 34, e2019GB006385. <https://doi.org/10.1029/2019GB006385>

Received 29 JUL 2019

Accepted 5 MAR 2020

Accepted article online 4 APR 2020

## The Simulated Biological Response to Southern Ocean Eddies via Biological Rate Modification and Physical Transport

Tyler Rohr<sup>1,2</sup> , Cheryl Harrison<sup>3,4,5</sup> , Matthew C. Long<sup>5</sup> , Peter Gaube<sup>6</sup> , and Scott C. Doney<sup>1,7</sup> 

<sup>1</sup>Department of Marine Chemistry and Geochemistry, Woods Hole Oceanographic Institution, Woods Hole, MA, USA, <sup>2</sup>Department of Earth and Planetary Sciences, Massachusetts Institute of Technology, Cambridge, MA, USA, <sup>3</sup>School of Earth, Environmental, and Marine Science, University of Texas Rio Grande Valley, Port Isabel, TX, USA, <sup>4</sup>Institute for Arctic and Alpine Research, University of Colorado Boulder, Boulder, CO, USA, <sup>5</sup>National Center for Atmospheric Research, Boulder, CO, USA, <sup>6</sup>Applied Physics Laboratory, University of Washington, Seattle, WA, USA, <sup>7</sup>Department of Environmental Sciences, University of Virginia, Charlottesville, VA, USA

**Abstract** We examine the structure and drivers of anomalous phytoplankton biomass in Southern Ocean eddies tracked in a global, multiyear, eddy-resolving, 3-D ocean simulation of the Community Earth System Model. We examine how simulated anticyclones and cyclones differentially modify phytoplankton biomass concentrations, growth rates, and physical transport. On average, cyclones induce negative division rate anomalies that drive negative net population growth rate anomalies, reduce dilution across shallower mixed layers, and advect biomass anomalously downward via eddy-induced Ekman pumping. The opposite is true in anticyclones. Lateral transport is dominated by eddy stirring rather than eddy trapping. The net effect on anomalous biomass can exceed 10–20% of background levels at the regional scale, consistent with observations. Moreover, we find a strong seasonality in the sign and magnitude of regional anomalies and the processes that drive them. The most dramatic seasonal cycle is found in the South Pacific Antarctic Circumpolar Current, where physical and biological processes dominate at different times, modifying biomass in different directions throughout the year. Here, in cyclones, during winter, anomalously shallow mixed layer depths first drive positive surface biomass anomalies via reduced dilution, and later drive positive depth-integrated biomass anomalies via reduced light limitation. During spring, reduced iron availability and elevated grazing rates suppress net population growth rates and drive the largest annual negative surface and depth-integrated biomass anomalies. During summer and fall, lateral stirring and eddy-induced Ekman pumping create small negative surface anomalies but positive depth-integrated anomalies. The same mechanisms drive biomass anomalies in the opposite direction in anticyclones.

## 1. Introduction

Surface chlorophyll anomalies in mesoscale eddies have been observed across the global ocean (Frenger et al., 2018; Gaube et al., 2015; Large, 1998; McGillicuddy et al., 2007) and are thought to dominate global spatiotemporal variability in phytoplankton distributions (Doney et al., 2003; Glover et al., 2018). The mechanisms driving this variability appear to be highly variable in both space and time and are hitherto not fully understood (Frenger et al., 2018; Gaube et al., 2014). The Southern Ocean, in particular, is characterized by strong mesoscale activity (Meredith, 2016) associated with a highly variable biological response (Frenger et al., 2018). Better understanding the mechanistic underpinning of eddy-modified phytoplankton populations is necessary to better understand the Southern Ocean's role in global biogeochemical cycling (Marinov et al., 2008; Siegel et al., 2014) and atmospheric carbon uptake (Hauck et al., 2015).

It is difficult to determine the mechanisms driving eddy-induced biogeochemical anomalies because eddies simultaneously modify the environment in a number of different ways (McGillicuddy, 2016) (Figure S1 in the supporting information). Southern Ocean cyclones, which are associated with a cold sea surface temperature anomaly ( $-SST'$ ) and negative sea surface height anomaly ( $-SSH'$ ), rotate clockwise, stratify the water column as they dome isopycnals (Dufois et al., 2014; Gaube et al., 2019; Hausmann et al., 2017), and

induce Ekman-downwelling as they alter the curl of the relative wind stress (Dewar & Flierl, 1987; Gaube et al., 2015). The opposite is true of anticyclones. Both cyclones and anticyclones trap water at their core as they propagate and stir water around their periphery as they rotate. The strength with which any particular mechanism can modify biology is sensitive to local environmental conditions such as the meridional chlorophyll gradient (Chelton, Schlax, and Samelson 2011; Frenger et al., 2018) or the depth of the winter mixed layer (Song et al., 2018). In the context of regional and basin-scale biogeochemical cycling, understanding variability in the mechanisms that drive phytoplankton biomass anomalies is fundamental to understanding whether eddies are actually stimulating or suppressing new production via biological mechanisms or only moving biomass around via lateral and vertical transport mechanisms.

Biological mechanisms in eddies can induce biomass anomalies from the bottom-up by modifying division rates as well as from the top-down by modifying loss rates (i.e., grazing, mortality, and sinking). In the Southern Ocean, division rates are limited by light (Nelson & Smith, 1991) and iron (Boyd, 2002; Carranza & Gille, 2015). Eddies can modify depth-averaged light and nutrient limitation by redistributing biomass and iron profiles. The relative effect of these mechanisms in simulated eddies was examined extensively in Rohr et al. (2020) and found to be dominated by the anomalous vertical transport of iron, leading to depressed division rates in cyclones and elevated division rates in anticyclones throughout most of the year. In the Southern Ocean, loss rates are predominantly driven by grazing (Deppeler & Davidson, 2017). Eddies can reduce grazing efficiency by reducing stratification and thereby diluting phytoplankton across anomalously deep mixed layers (Behrenfeld et al., 2013).

Lateral transport mechanisms can induce biomass anomalies by advecting biomass across a horizontal gradient as an eddy rotates or propagates. Lateral transport can modify both surface and depth-integrated biomass provided that the scale of the background gradient is large relative to the spatial scale of the eddy (10–100 km; Frenger et al., 2015), and the timescale of advection is faster than that of the relaxation of large-scale anomalies. Eddy stirring is the process by which eddies disturb the background gradient as they rotate, typically with timescales of days to weeks (Chelton, Schlax, and Samelson 2011). Eddy trapping is the process by which nonlinear eddies (i.e., those with a rotational speed faster than their propagation speed Flierl, 1981) trap and transport water at their core as they propagate (Early et al., 2011; Flierl, 1981; Lehahn et al., 2011). Propagation speeds in Southern Ocean eddies are typically an order of magnitude lower than their rotational speeds, meaning that the majority are nonlinear (Chelton, Gaube, et al., 2011) and also implying that they do not propagate very far (Frenger et al., 2015). In turn, lateral stirring tends to dominate relative to trapping in Southern Ocean chlorophyll observations (Chelton, Schlax, and Samelson 2011, Frenger et al., 2018).

Vertical transport mechanisms in eddies can induce surface biomass anomalies by redistributing biomass in the water column. In cyclones, increased near-surface stratification can lead to shallower mixed layer depths (Dufois et al., 2016; Hausmann et al., 2017), reduced dilution, and anomalously high surface biomass concentrations, while eddy-induced Ekman downwelling can advect biomass to depth and lead to anomalously low surface concentrations. Finally, upwelling induced by eddy pumping during the formation of cyclones (Falkowski et al., 1991) could increase surface concentrations if there is biomass at depth to advect upward. The opposite is true in anticyclones.

The variety of physical and biological mechanisms helps explain why there is such a high degree of spatiotemporal variability in anomalous biomass within eddies throughout the Southern Ocean (Frenger et al., 2018) and the world at large (Gaube et al., 2014). For example, in the South Pacific Antarctic Circumpolar Current (ACC) observations (Dawson et al., 2018; Frenger et al., 2018; Song et al., 2018) and simulations (Song et al., 2018) agree that eddies exhibit a seasonal flip in the sign of surface chlorophyll anomalies during the winter. Frenger et al. (2018) point out that this seasonal reversal cannot be explained by either stirring or trapping and hypothesize that it must be attributed to a combination of modifications to light availability, iron limitation, and grazing efficiency (Carranza & Gille, 2015; Le Quéré et al., 2016; Smetacek et al., 2004), but they lacked the observational capacity to constrain these processes. Song et al. (2018) employed a numerical simulation to examine depth-integrated light and iron limitation and concluded that this flip is controlled by eddy-modified light availability, but did not explicitly examine division rates, net population growth rates, or dilution. Using the same numerical integration employed by Song et al. (2018), Rohr et al. (2020) confirmed that this flip is, in fact, associated with a coincident reversal in the direction of division rate anomalies, but the degree to which physical dilution and/or elevated loss rates driven by improved grazing

efficiency (Behrenfeld et al., 2013) contribute was not addressed. Moreover, it remains unclear how physical and biological mechanisms more generally interact to modify biomass throughout the Southern Ocean.

Here we employ the same numerical simulation as Song et al. (2018) and continue to analyze the same set of simulated Southern Ocean eddies that were identified and tracked in Rohr et al. (2020). We examine spatiotemporal variability in surface and depth-integrated biomass anomalies within eddies (section 3.1) and the eddy-induced mechanisms that drive a biological response in phytoplankton net population growth rates (section 3.2) while simultaneously physically transporting biomass (section 3.3). In addition to broadly characterizing eddies over the entire Southern Ocean, specific focus is dedicated to the South Pacific, where eddies exhibit the most coherent signal (Song et al., 2018), consistent zonal structure, and the deepest winter mixing. Large South Pacific eddies within the ACC are further highlighted because they exhibit the most dramatic seasonal cycle, featuring a seasonal reversal in the direction of anomalous biomass (Frenger et al., 2018; Song et al., 2018). The vertical structure of this seasonal cycle is examined in section 3.4 before we discuss which mechanisms drive these anomalies in section 4.1. Finally, we consider the overall effect of regional and basin-scale biomass anomalies in section 4.2. Complete Southern Ocean distributions of various eddy-modified anomaly fields are provided for reference in supporting information Figures S3–S14.

## 2. Methods

### 2.1. Numerical Simulation

We analyze a global, multiyear, eddy-resolving, 3-D numerical simulation integrated with the ocean, ice, and biogeochemistry components of the Community Earth System Model 1. The physical ocean simulation is Parallel Ocean Program Version 2 (Smith et al., 2010), vertical mixing is based on the K-Profile Parameterization (Large et al., 1994), sea ice is treated using CICE4 (Hunke & Lipscomb, 2008), and biogeochemistry is treated with the Biogeochemical Element Cycle model (Moore et al., 2013). The simulation was forced with atmospheric data from the Coordinated Ocean-ice Reference Experiment I “normal year” (Griffies et al., 2009; Large & Yeager, 2004) and run for 5-years after initialization (see Harrison et al., 2018, for details on initialization), with model output saved as 5-day means. This is the same simulation employed in Rohr et al. (2020) and each component is described in greater detail there.

Within Biogeochemical Element Cycle, phytoplankton carbon biomass,  $C_{phyto}$  (mmol C), is resolved for three phytoplankton pools: diatoms, small phytoplankton, and diazotrophs. The carbon biomass concentration of each pool,  $[C_{phyto}]$  (mmol C/m<sup>3</sup>), is independently modified by biological rate terms as it is simultaneously mixed and advected by the physical ocean model. Global solutions integrated at a coarser resolution have been widely validated against global data sets and shown to capture basin-scale spatial distributions in productivity, chlorophyll concentrations (Doney et al., 2009; Moore et al., 2004, 2013), and carbon cycling (Lima et al., 2014; Long et al., 2013; Moore et al., 2013). More recently, this exact high resolution simulation has been shown replicate observations of seasonal variability in the distribution of mesoscale surface chlorophyll anomalies in the ACC (Song et al., 2018).

#### 2.1.1. Rate-Based Modification of Biomass

Class-specific phytoplankton net population growth ( $\frac{d[C_{phyto}]}{dt}$ ) is governed by a photosynthetic net primary productivity term,  $P_{phyto}$  (mmol C/m<sup>3</sup> day), and opposed by a loss term,  $L_{phyto}$  (mmol C/m<sup>3</sup> day), such that

$$\frac{d[C_{phyto}]}{dt} = P_{phyto} - L_{phyto}. \quad (1)$$

$P_{phyto}$  is composed of a volumetric specific division rate,  $\mu_{phyto}$  (day<sup>-1</sup>), multiplied by the biomass concentration ( $P_{phyto} = \mu_{phyto} * [C_{phyto}]$ ). The  $\mu_{phyto}$  is governed by temperature dependence, multinutrient limitation, and light availability and is described in detail in Rohr et al. (2020). Southern Ocean division rates are predominantly limited by light (Fauchereau et al., 2011) and iron (Boyd, 2002). This simulation is able to reproduce basin-wide distributions of iron (Moore & Braucher, 2008) and realistic Southern Ocean mixed layer depths, which control effective light availability (Harrison et al., 2018). In turn, simulated population specific division rates are within the observed range (Sakshaug & Holm-Hansen, 1986; Spies, 1987; Smith et al., 1999).

$L_{phyto}$  (mmol C/m<sup>3</sup> day) is composed of a volumetric specific loss rate,  $l_{phyto}$  (day<sup>-1</sup>), multiplied by the biomass concentration ( $L_{phyto} = l_{phyto} * [C_{phyto}]$ ). The  $l_{phyto}$  is composed of a nonlinear grazing rate,  $gr_{phyto}$  (day<sup>-1</sup>), a linear mortality rate ( $mort_{phyto}$  (day<sup>-1</sup>), and a quadratic mortality/aggregation rate.

The nonlinear grazing term, which dominates losses in the Southern Ocean (Deppeler & Davidson, 2017), is governed by a temperature dependent, nonlinear function (Holling Type III Holling, 1959) of the phytoplankton concentration such that zooplankton become more efficient grazers as phytoplankton concentrations increase,

$$g r_{phyto} = \mu_{zoo:phyto}^{max} * L_T * \left( \frac{[C_{phyto}]^2}{[C_{phyto}]^2 + g_{phyto}^2} \right) * [Z_C], \quad (2)$$

where  $\mu_{zoo:phyto}^{max}$  ( $\text{day}^{-1}$ ) is the maximum zooplankton specific grazing rate on phytoplankton class *phyto*,  $L_T$  is the dimensionless temperature dependency term,  $g_{phyto}$  is the zooplankton grazing coefficient ( $\text{mmol C/m}^3$ ), and  $[Z_C]$  is the zooplankton carbon biomass concentration ( $\text{mmol C/m}^3$ ). The parameterization of grazing in global climate models is still a topic of ongoing debate (Laufkötter et al., 2015; Le Quéré et al., 2016; Saille et al., 2013). However, the nature of the mechanistic pathways described here hinges more on the grazing functional form than the specific values of parameterized terms. Nonlinearities in the simulated predator-prey relationship (Holling, 1959) ensure that zooplankton become more efficient grazers as the concentration of phytoplankton increases. Still, this grazing framework does not include discrete aspects of zooplankton life history like diapause, where grazing completely shuts down in the winter (Fiksen, 2000; Varpe, 2012), regardless of the mixed layer depth or degree of dilution, which could mitigate the effect of eddy-induced mixing anomalies on dilution-driven modifications to net population growth rates.

All together, the volumetric specific net population growth rate,  $r_{phyto}$  ( $\text{day}^{-1}$ ) is equal to the difference between the specific division rate and loss rate,

$$r_{phyto} = \mu_{phyto} - l_{phyto}. \quad (3)$$

Simulated population specific net growth rates are within the observed range (Boyd et al., 2001).

### 2.1.2. Physical Transport of Biomass

The physical transport of biomass is dominated by fluxes ( $\text{mmol C/m}^2/\text{s}$ ) from horizontal advection ( $U_{phyto}, V_{phyto}$ ), vertical advection ( $W_{phyto}$ ), and vertical diabatic mixing ( $Mix_{phyto}$ ). All flux terms are averaged over the 5-day time step over which model output is saved. Vertical fluxes are positive in the upward direction.

## 2.2. Model Analysis

### 2.2.1. Biomass

The majority of observations (i.e., Gaube et al., 2014, Frenger et al., 2018) and modeling work (i.e., Gaube & McGillicuddy, 2017; Song et al., 2018) have focused on how eddies modify surface populations. Unfortunately, surface concentrations may not always be a good indicator of the depth-integrated biomass inventory (Carranza et al., 2018; Rohr et al., 2017) because of dilution during deep mixing (Behrenfeld et al., 2013), biomass that may exist below a shallow mixed layer (Behrenfeld et al., 2013), or the potential of nonuniform profile distributions (McGillicuddy et al., 2007; Siegel et al., 1999). In addition to considering surface concentrations ( $[C_{phyto}]_S$ ), here we also focus on depth-integrated biomass inventories ( $\Sigma C_{phyto}$ ) and profiles of depth-resolved concentrations ( $[C_{phyto}]_z$ ). In all cases biomass is integrated over the two regionally dominant phytoplankton pools: diatoms and small phytoplankton.

### 2.2.2. Biological Rate Terms

Biological rate terms are expressed both as depth-resolved values ( $\mu_z, l_z, r_z$ ) and biomass-weighted, depth-averaged values ( $\mu_\Sigma, l_\Sigma, r_\Sigma$ ), such that

$$\mu_\Sigma = \sum_{z=0m}^{water\ column} \sum_{phyto=sp,diat} \mu_{z,phyto} \frac{[C_{phyto}]_z * h}{\Sigma C_{phyto}}, \quad (4)$$

$$l_\Sigma = \sum_{z=0m}^{water\ column} \sum_{phyto=sp,diat} l_{z,phyto} \frac{[C_{phyto}]_z * h}{\Sigma C_{phyto}}, \quad (5)$$

$$r_\Sigma = \sum_{z=0m}^{water\ column} \sum_{phyto=sp,diat} r_{z,phyto} \frac{[C_{phyto}]_z * h}{\Sigma C_{phyto}}, \quad (6)$$

where  $[C_{phyto}]_z$  is the biomass concentration at a given grid cell and depth (mmol C/m<sup>3</sup>),  $h$  is the height of the grid cell (m), and the  $\Sigma C_{phyto}$  is the depth-integrated sum of diatom and small phytoplankton biomass (mmol C/m<sup>2</sup>). Biomass-weighted, depth-averaged rate terms describe the effective population-specific rate terms for the full column inventory in a manner that is consistent with the time evolution of the vertical biomass profile and depth variability in division and loss rates.

Biomass-weighted, depth-averaged rate terms are needed to capture the complete biological response to eddy perturbation, which can both modify the vertical profiles of growth conditions (e.g., iron availability) as well as the vertical distribution of phytoplankton subject to those conditions. It is important to capture, for example, what percent of the depth-integrated phytoplankton population has access to eddy-enhanced iron at depth. By representing the mean state of the entire column-integrated phytoplankton population, results are sensitive to eddy-modified variability in the vertical distribution of growth conditions, biomass, and community composition, while accounting for dilution during deep mixing (Behrenfeld et al., 2013; Rohr et al., 2017) and the possibility of nonuniform biomass profiles or subsurface maxima (McGillicuddy et al., 2007; Siegel et al., 1999).

### 2.2.3. Vertical Transport Mechanisms

We examine depth-resolved profiles of the diabatic mixing flux of carbon biomass,  $MIX_C$  (mmol C/m<sup>2</sup>/s), and the vertical advection flux of carbon biomass,  $W_C$  (mmol C/m<sup>2</sup>/s), as well as the flux into the surface ocean (1–10 m). Surface fluxes are expressed as  $MIX_{C,s}$  (mmol C/m<sup>2</sup>/s) and  $W_{C,s}$  (mmol C/m<sup>2</sup>/s), respectively. The vertical velocity of eddy-induced Ekman pumping,  $\Omega_{Ek}$  (m/s), is estimated diagnostically from the curl of the relative surface stress and described in detail in Rohr et al. (2020).

Regarding vertical mixing, this specific simulation has been shown to capture deeper, more realistic winter mixed layers and improved spatial patterns throughout the Southern Ocean (Harrison et al., 2018) relative to other simulations. However, it does not produce the same asymmetry in observed eddy-induced mixed layer depth anomalies reported by Hausmann et al. (2017). The simulation overestimates the magnitude of cyclonic anomalies (Rohr et al., 2020). The implication of this on basin-scale anomalous biomass is addressed in section 4.2. Regarding vertical advection the simulation accurately captures the net upwelling observed in Southern Ocean (Morrison et al., 2014; Tamsitt et al., 2017). The simulated eddy demographics that drive eddy-induced Ekman pumping (e.g., size and speed) compare well with observations (Rohr et al., 2020).

### 2.2.4. Lateral Transport Mechanisms

Explicitly prescribing the effects of lateral transport is complicated by dynamic and permeable eddy boundaries, simultaneous internal modifications, interactions with other mesoscale features, and a Lagrangian reference frame. Here, we estimate the maximum potential for an anomaly to be created by an isolated eddy moving across the climatologic field. Following Frenger et al. (2018), the size and direction of this potential anomaly can be constrained by the size and direction of the biomass gradient and the size, polarity, and propagation path of the eddy in question. Both, Southern Ocean chlorophyll distributions (Harrison et al., 2018) and eddy demographics (e.g., radius and propagation) (Rohr et al., 2020), are reproduced favorably in this simulation. This approximation allows for the scale of anomalies that could be induced by lateral processes to be compared to the biological and vertical sources of anomalous biomass.

Briefly, the trapping potential (*TRAP*) represents the anomaly that would be created if source water at the eddy's origin was adiabatically trapped and transported across the climatologic biomass field with perfect efficiency. This represents an upper bound, as eddies exchange some degree of water with their surroundings as they propagate, even if they are nonlinear (Beron-Vera et al., 2013; Haller, 2015). The trapping potential is computed by subtracting the biomass climatology at the time and location of any realization ( $t = i; x = i$ ), from the biomass climatology at the same time ( $t = i$ ) but at the location of eddy formation ( $x = 1$ ), such that

$$Biomass\ TRAP = \overline{Biomass}_{Clim, x=1, t=i} - \overline{Biomass}_{Clim, x=i, t=i}. \quad (7)$$

The stirring potential (*STIR*) represents the maximum anomaly related to an asymmetric dipole created by rotational stirring across westward propagating eddies, in which only the leading edge modifies undisturbed waters (Chelton, Schlax, and Samelson 2011; Frenger et al., 2018). This represents an upper bound because there will be some degree of averaging across the footprint of the eddy. The magnitude of this anomaly is estimated by multiplying the magnitude of the meridional gradient by the diameter of the eddy. Stirring across zonal gradients is not considered; however, in the open Southern Ocean, far from coastal boundary

currents, zonal gradients are much weaker than meridional gradients. The direction of the anomaly is prescribed based on the polarity of the eddy, direction of the gradient, and an assumed westward propagation relative to the mean flow (Frenger et al., 2018).

### 2.3. Depth Extrapolation

Some model output is extrapolated at depth, as storage limitations prevent saving the full-depth profiles of all prognostic tracers. In this simulation, biomass, biological rate terms, and light and iron limitation terms were archived to 150 m. If the mixed layer depth (*MLD*) is shallower than 150 m it is reasonable to assume that biomass below 150 m cannot access the euphotic depth (~100 m) and is likely negligible. In turn, we assume biomass concentrations are zero below 150 m if *MLD* < 150 m. During the winter though, deep mixing can penetrate well below 150 m. In order to diagnostically characterize biomass beneath what has been explicitly saved during deep mixing events (*MLD* > 150 m), all relevant profiles are linearly extrapolated to the base of the *MLD* and assumed to drop to 0 immediately below the *MLD*. Southern Ocean observations support the approximation of an uniform biomass profiles across deep winter mixed layers (Uitz et al., 2006).

### 2.4. Anomaly and Climatology Fields

Anomaly and climatology fields were created identically to those described in Rohr et al. (2020). A detailed description of smoothing techniques and justification of filter size can be found there. Briefly, spatial anomaly fields for each relevant variable ( $var'$ ) are computed by removing the mean field ( $\overline{var}$ ) from the raw field ( $var$ ), such that

$$var' = var - \overline{var}. \quad (8)$$

Mean fields were created by smoothing the raw fields with a 2-D low-pass loess filter. Background climatology fields ( $\overline{var}_{clim}$ ) were computed by averaging each year day of model output (saved as 5-day averages) across the 5 years of simulation and then smoothing those fields in time and space. Anomaly fields were divided by the corresponding climatology to create normalized anomaly fields ( $var''$ ).

$$var'' = \frac{var'}{\overline{var}_{clim}}. \quad (9)$$

### 2.5. Eddy Identification and Tracking

The complete set of Southern Ocean eddies analyzed here is identical to those analyzed in Rohr et al. (2020). Eddies were identified and tracked as closed contours in the SSH anomaly ( $SSH'$ ) field using the parameter less algorithm originally developed by Chelton, Gaube, et al. (2011) and adapted by Faghmous et al. (2015). Each simulated eddy track is composed of eddy “realizations” identified at 5-day intervals. The distribution and demographics of observed eddy tracks from Chelton, Gaube, et al. (2011) compare favorably to those of simulated tracks, particularly north of the marginal ice zone (see Rohr et al., 2020). All variables are averaged over the lateral footprint of each eddy realization. An eddy variable is referred to as anomalously high (low) if the mean anomaly of all grid cells within the eddy is greater (lesser) than 0.

### 2.6. Eddy Subsets and Composite Averages

The Southern Ocean is defined from the pole to 40°S (e.g., Figures S3–S14 and 3a–3c). Eddies are said to be in the South Pacific (e.g., Figures 1–8) if they are found between 80°W < Lon < 180°W and are south of 40°S. Eddies are said to be in the ACC (e.g., Figures 3d and 3e, 6, and 8) if they are within the  $-20$  and  $-80$  cm *SSH* contours (Frenger et al., 2018), defined dynamically by the daily *SSH* climatology ( $\overline{SSH}_{clim}$ ). Eddies are referred to as large if their radius is greater than 50 km and their  $SSH'$  amplitude is greater than 5 cm.

Eddy composite averages displayed in Figures 1–6 are averaged across all eddy realizations that fall within a given spatiotemporal bin. Composite anomalies are considered statistically significant if a one-sample *t* test rejects the null hypothesis that the sample set of eddy anomalies in a given bin comes from a normally distributed population with mean equal to 0 at the 95% confidence level.

## 3. Results

### 3.1. Anomalous Biomass in Eddies

#### 3.1.1. Anomalous Surface Biomass

Throughout the Southern Ocean, surface biomass concentrations ( $[C_{phyto}]_s$ ) are anomalously high in roughly half of all cyclones and roughly half of all anticyclones, with a high degree of variability in the size

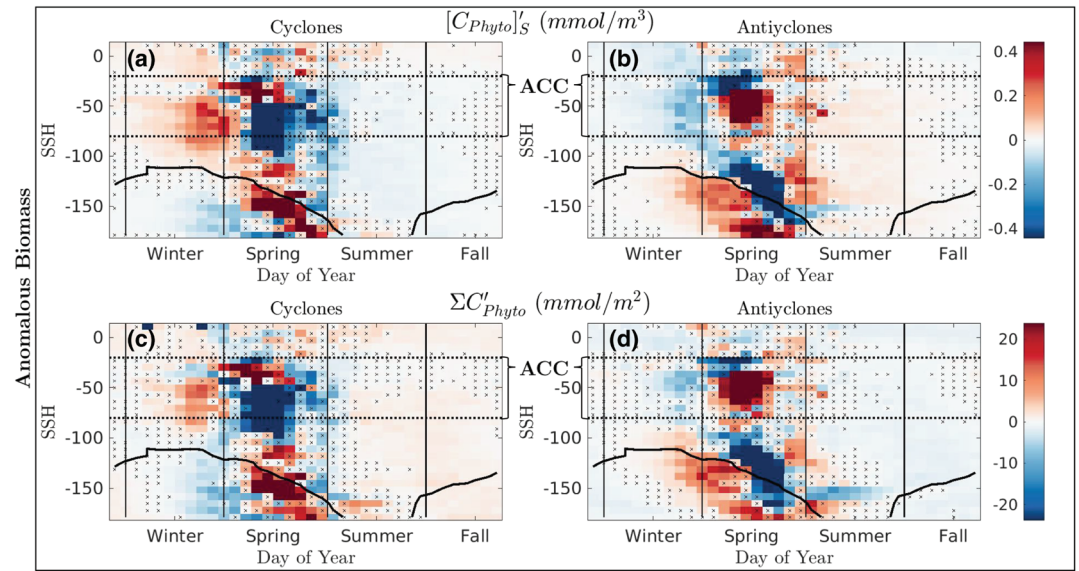


**Figure 1.** Composite averaged annual cycle of anomalous biomass in South Pacific eddies. Anomalous (a, b) surface biomass concentrations ( $[C_{Phyto}]'_S$ ), and (c, d) depth-integrated biomass inventories ( $\Sigma C'_{Phyto}$ ) are plotted for cyclones (on the left) and anticyclones (on the right). Anomalies are plotted as a function of season and SSH. SSH serves as dynamic proxy for latitude to help align meanders in the ACC during zonal averaging. Only eddies in the Pacific sector ( $80^\circ\text{W} < \text{Lon} < 180^\circ\text{W}$ ) of the Southern Ocean ( $\text{Lat} < 40^\circ\text{S}$ ) are included. The climatologic ice edge ( $\text{Ice Fraction} > 80\%$ ) is overlaid with a solid black contour. The ACC is denoted with dashed horizontal lines. Composite anomalies are averaged across all eddy realizations that fall within a given bin, with the upper and lower 5% of values excluded. Composite anomalies are considered statistically significant if a one-sample  $t$  test rejects the null hypothesis that the sample set of eddy anomalies in a given bin comes from a normally distributed population with mean equal to 0 at the 95% confidence level. Bins that are not statistically significant are denoted with a black x.

and direction of anomalies, regardless of polarity (Figure S3 and Table S1). However, cyclones and anticyclones rarely modify surface biomass in the same direction at the same time in the same region. Instead, surface biomass within cyclones and anticyclones in spatial-temporal proximity is typically modified in opposite directions, but by a similar magnitude.

The most coherent seasonal variability occurs in the South Pacific, especially in the ACC (Figures 1a and 1b). Within South Pacific ACC cyclones, surface biomass is generally elevated during the winter and depressed during the spring (Figure 1a). The largest magnitude anomalies occur in the late winter and spring, when surface biomass can be elevated by upwards of 20% of background climatologic values. The opposite is generally true in anticyclones (Figure 1b). In terms of phenology, this can shift the spring bloom earlier in cyclones relative to anticyclones. After the spring bloom subsides, surface biomass is relatively depressed in cyclones and elevated in anticyclones, but the magnitude of these anomalies is largely reduced in the summer and fall. North of the ACC, the signal is less consistent, and often statistically insignificant. South of the ACC, the seasonal cycle is generally reversed and associated with the advance and retreat of sea ice.

### 3.1.2. Anomalous Depth-Integrated Biomass

Throughout the Southern Ocean the direction of the anomalous depth-integrated biomass inventory ( $\Sigma C'_{Phyto}$ ) is often consistent with the anomalous surface biomass concentration, particularly during the late winter and spring when anomalies are the largest (Figure S4 and Table S1). During this period the effects of eddies on surface and depth-integrated biomass are well coupled, although the magnitude of anomalous depth-integrated biomass is not as large as anomalous surface biomass relative to background conditions, with winter and spring time anomalies reaching 5–10% of climatologic values.

In the South Pacific there are two instances where surface and depth-integrated biomass are not well-coupled (Figures 1c and 1d). The first is in South Pacific ACC eddies during the early winter, while the mixed layer is deepening, when surface biomass anomalies become statistically significant prior to depth-integrated biomass anomalies. This decoupling is tied to physical dilution (see section 4.1.1). The

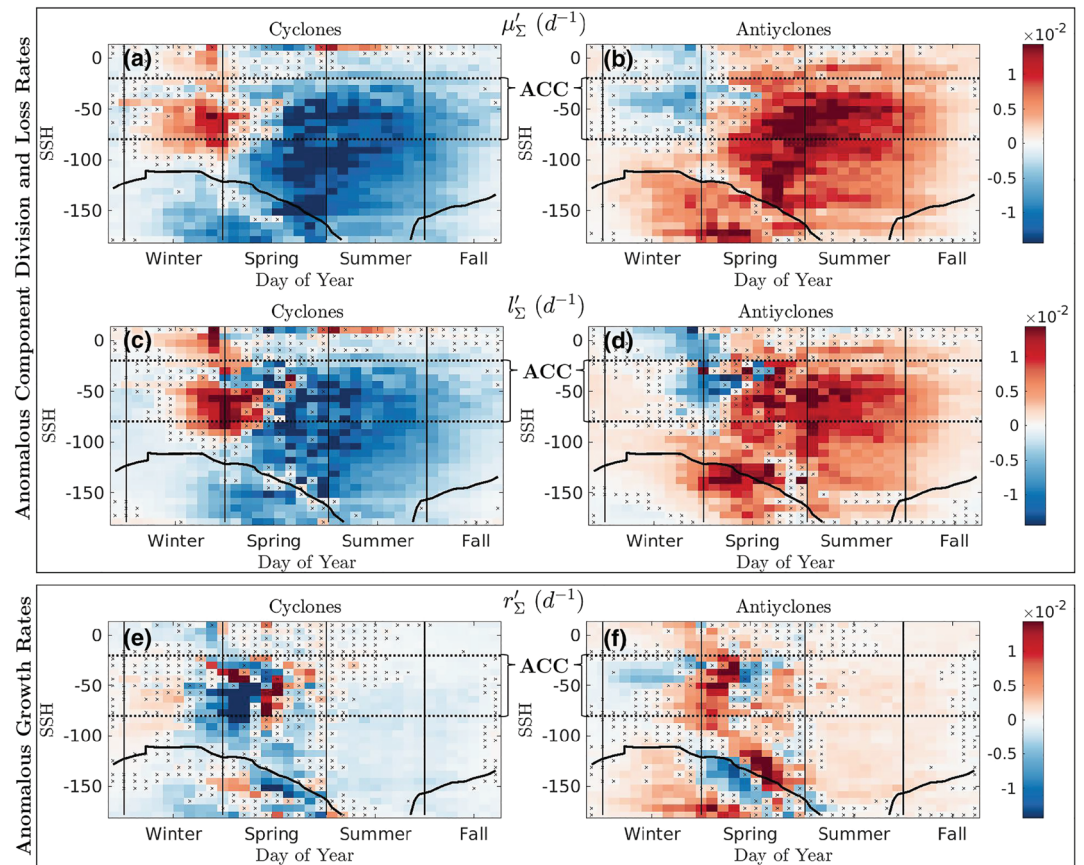


**Figure 2.** Composite averaged annual cycle of anomalous biological rate terms in South Pacific eddies. Identical to Figure 1 but for anomalous biomass-weighted, depth-averaged, population-specific (a, b) division rates ( $\mu'_{\Sigma}$ ), (c, d) loss rates ( $l'_{\Sigma}$ ), and (e, f) net population growth rates ( $r'_{\Sigma}$ ).

second exception is in South Pacific eddies during the fall and summer, where surface and depth-integrated biomass are consistently modified in different directions. This decoupling is tied to eddy-induced Ekman pumping (see section 4.1.3). However, in the late winter and spring, when biomass anomalies are the largest, depth-integrated and surface biomass anomalies are well-coupled and tied to eddy-modified depth-integrated net population growth rates (see section 4.1.2).

### 3.2. Anomalous Phytoplankton Net Population Growth Rates in Eddies

#### 3.2.1. Division Rates

Throughout the Southern Ocean, simulated biomass-weighted, depth-averaged, division rates ( $\mu_{\Sigma}$ ) are generally depressed in cyclones and elevated in anticyclones with magnitudes roughly 5–10% of background climatologic values (Figure S5 and Table S1). This is clearly evident in the South Pacific throughout the majority of the year, with the exception of eddies within the ACC in the winter deep mixing period when the sign of anomalies is reversed (Figures 2a and 2b). Eddy-modified division rates are predominantly driven by an anomalous advective flux of iron transported via anomalous eddy-induced Ekman pumping (Rohr et al., 2020). However, the seasonal flip in sign is associated with large mixed layer depth anomalies in which anomalous light availability is large enough to compensate for the coincident, competing effect of anomalous iron availability. See Rohr et al. (2020) for a detailed description of the mechanistic drivers controlling anomalous division rates.

#### 3.2.2. Loss Rates

Throughout the Southern Ocean, simulated biomass-weighted, depth-averaged, loss rate anomalies ( $l'_{\Sigma}$ ) are generally well correlated with division rate anomalies (Figure S6 and Table S1). Anomalous loss rates are composed of contributions from eddy-modified grazing (Figure S7), mortality (Figure S8), and aggregation (Figure S9) but are driven primarily by eddy-modified grazing rates. Anomalous grazing rates are an order of magnitude larger than the other terms (Figure S2) and much better correlated with anomalous loss rates

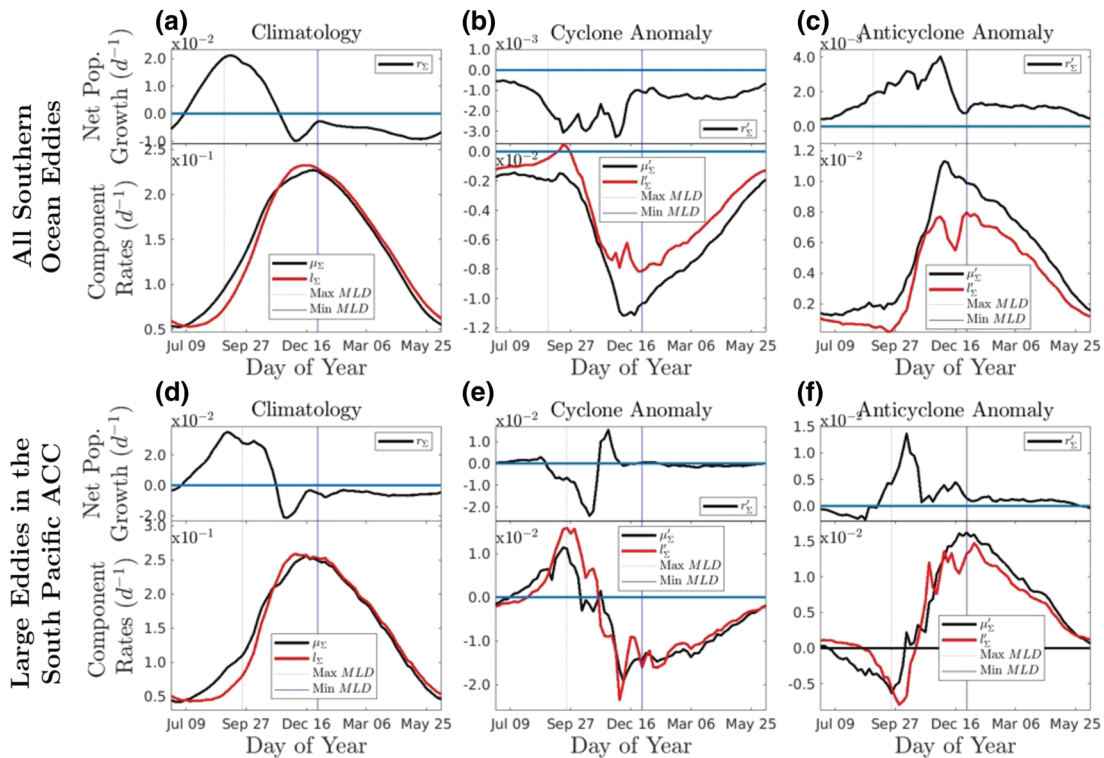


**Figure 3.** Seasonal evolution of rate terms. The seasonal evolution of (a, d) climatologic and anomalous (b, c, e, and f) population averaged rate terms is provided for (a–c) the average of all Southern Ocean eddies as well as (d–f) the subset of only large South Pacific eddies within ACC. (a, d) Climatologies, (b, e) cyclone anomalies, and (c, f) anticyclone anomalies are provided from left to right. Each panel is broken into the evolution of component rate terms ( $\mu'_\Sigma$  in black;  $l'_\Sigma$  in red) on the bottom and the net population growth rate ( $r'_\Sigma$  in black) on the top. The day of the climatologic mixed layer depth maximum and minimum is denoted with dashed and solid vertical blue lines, respectively.

( $r = 0.98$ ). Eddies influence grazing efficiency via processes that modify phytoplankton biomass concentrations. In turn, anomalous grazing rates are positively correlated with anomalous division rates, which increase biomass concentrations ( $r = +0.69$ ), and negatively correlated with mixed layer depth anomalies in deep mixing winter ACC eddies, which dilute biomass concentrations ( $r = -0.51$ ). The tight coupling between anomalous division and loss rates is clear in Southern Pacific eddies (Figures 2a–2d).

### 3.2.3. Net Population Growth Rates

Throughout the Southern Ocean, biomass-weighted, depth-averaged, net population growth rates ( $r_\Sigma$ ) are generally depressed in cyclones and elevated in anticyclones, with typical magnitudes of 1–3% of background climatologic values (Figure S10 and Table S1). Anomalous net population growth rates are driven by the competing effects of anomalous division and loss rates ( $r'_\Sigma = \mu'_\Sigma - l'_\Sigma$ ) but are, on average, dominated by the effect of eddy-modified division rates. This is possible even though anomalous division rates and loss rates are generally well coupled ( $r = 0.73$ ; Table S2) because anomalous division rates typically lead and exceed anomalous loss rates by a small margin, driving net population growth rates down in cyclones and up in anticyclones. Averaged across all Southern Ocean eddies, the seasonal cycle of eddy-modified rate anomalies shows that even though the sign of anomalous division rates and loss rates is the same, the magnitude of anomalous division rates is consistently larger (Figures 3a–3c). In turn, the seasonal cycle of anomalous net population growth rates qualitatively resembles that of anomalous division rates, with both coincidentally peaking in magnitude, shortly before the background MLD shoals to its annual minimum. The positive correlation between anomalous division rates and anomalous net population growth rates suggests a strong bottom-up control in which the effect of eddies on the factors that modify division rates (e.g., light and iron) (Rohr et al., 2017) dominate those that modify loss rates (e.g., dilution).

In the South Pacific, eddy-modified net population growth rates are also often controlled by anomalous division rates, typically leading to depressed net population growth rates in cyclones and elevated net population growth rates in anticyclones (Figures 2e and 2f). However, the seasonal cycle within large eddies

in the South Pacific ACC is more complex (Figures 3d–3f). Here, during most of the winter, when modified light availability drives a reversal in the direction of division rate anomalies, net population growth rate anomalies follow suit, consistent with a bottom-up control. However, during late winter mixing and subsequent spring shoaling there is a period of top-down control, in which the effect of eddies on loss rates dominates their effect on division rates. Here, the magnitude of anomalous loss rates exceeds that of division rates, briefly driving anomalous net population rates in the opposite direction of anomalous division rates. Eventually, by the time the mixed layer has shoaled, a bottom-up control returns and division and net population growth rates are modified in the same direction throughout the summer and fall.

### 3.3. Anomalous Physical Transport of Phytoplankton Biomass in Eddies

#### 3.3.1. Horizontal Stirring and Trapping

The potential for eddies to induce an anomaly by stirring biomass across a background gradient as they rotate ( $[C_{\text{phyto}}]_S$  *STIR*) is much larger than the potential to induce an anomaly by trapping biomass at their core as they propagate ( $[C_{\text{phyto}}]_S$  *TRAP*). The magnitude of potential anomalies induced by horizontal transport is similar in size to their associated biomass anomalies; however, the actual effects of stirring and trapping are likely less pronounced, as the potential computed here represents an upper bound (see section 2.2.4).

Throughout the Southern Ocean the direction of biomass anomalies that can be induced by stirring is necessarily opposite in colocated cyclones and anticyclones due to the direction of their rotation, but there is a great degree of spatial-temporal variability in the size and direction of the stirring potential following variability in the background biomass gradient (Figure S11). For example, in the South Pacific, large spring blooms in the ACC and marginal ice zone lead to large meridional gradients and the largest potential for an anomaly to form via lateral stirring (Figures 4a and 4b). During the spring, the size of this potential anomaly can reach 10–20% of background climatologic values. In westward propagating cyclones, which rotate clockwise, the anomaly is expected to be positive where the background gradient is increasing north to south (Figures 4a and S11). The opposite is true in anticyclones (Figures 4b and S11).

Eddies can also transport biomass via trapping, but the potential (Figure S12) is consistently less than that of the stirring potential (Figure S11) and more often statistically insignificant. For example, in the South Pacific, the potential influence of trapping is either very small or statistically insignificant throughout much of the year (Figures 4c and 4d). This is because simulated Southern Ocean eddies do not typically propagate far from where they originate, which is consistent with observations (Frenger et al., 2015). Where the potential for trapping is statistically significant (e.g., the springtime ACC), it generally operates in the same direction as stirring, but with a much lower potential magnitude.

Trapping in ACC cyclones typically has the potential to induce an anomaly in the same direction as stirring because ACC cyclones have a disproportionate tendency to propagate northward relative to anticyclones in this simulation. This is consistent with observations by Frenger et al. (2015) that cyclones are more likely to pinch off ACC fronts to the north. In turn, the northward propagation of cyclones across a meridional gradient should induce the same sign anomaly as the westward propagation and clockwise rotation across the same meridional gradient (Frenger et al., 2018). The opposite logic applies to anticyclones.

#### 3.3.2. Vertical Transport

##### 3.3.3. Vertical Mixing

Eddies with anomalous mixed layer depths can physically mix biomass to different depths than surrounding waters via an anomalous diabatic vertical mixing flux ( $Mix'_C$ ). The anomalous vertical mixing flux is generally upward ( $+Mix'_C$ ) in eddies with anomalously shallow mixed layer depths and downwards ( $-Mix'_C$ ) in eddies with anomalously deep mixed layer depths. This is because the biomass profile generally has a downward concavity, meaning that active vertical mixing works to smooth the vertical gradient by mixing high surface concentrations down to depth. Note that an anomalously upward mixing flux does not necessarily mean there is an upward flux of biomass, just a smaller downward flux relative to surrounding waters. Throughout the Southern Ocean, cyclones, especially large cyclones in waters with deep background mixed layer depths, typically exhibit anomalously shallow mixed layer depths (Rohr et al., 2020) and typically induce an anomalously upward mixing flux into the surface (Figure S13). The opposite is true in anticyclones.

In the South Pacific ACC, where winter mixing is deep, winter anticyclones mix more biomass deeper into the water column while cyclones concentrate more biomass closer to the surface relative to surrounding waters. During the winter and early spring, large anomalous mixed layer depths in South Pacific ACC eddies

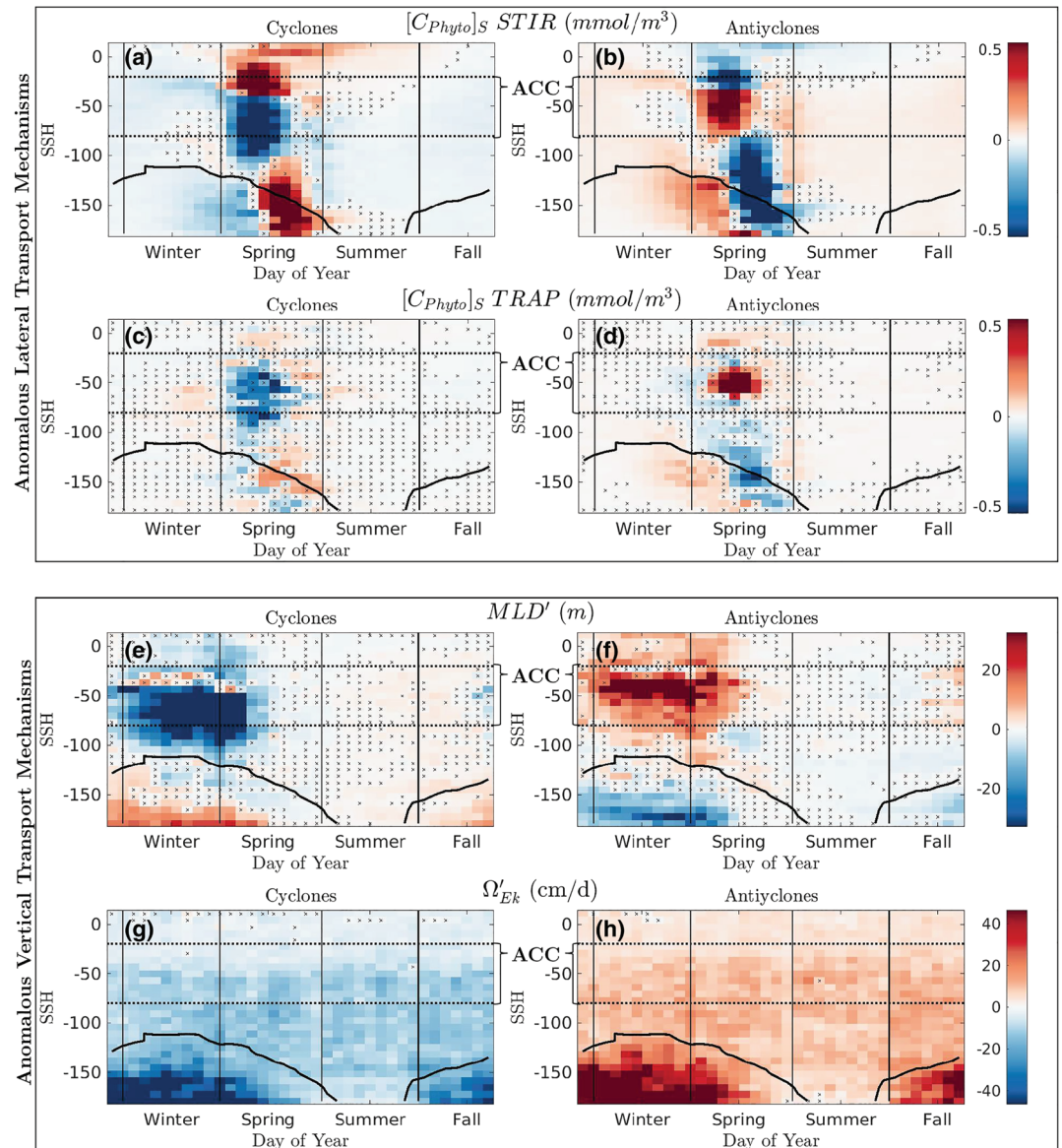


**Figure 4.** Composite averaged annual cycle of anomalous physical transport mechanisms in South Pacific eddies. Identical to Figure 1 but for physical transport mechanisms. Above, the potential surface biomass anomalies that could arise from (a, b) stirring (*STIR*) and (c, d) trapping (*TRAP*) characterize the lateral transport mechanisms. Below, anomalous (e, f) mixed layer depths (*MLD'*) and (g, h) eddy-induced Ekman pumping velocities ( $\Omega'_{Ek}$ ) characterize the vertical transport mechanisms.

(Figures 4e and 4f), often upward of 20% of climatologic values, drive a large anomalous vertical mixing flux of biomass into the surface ocean, often upwards of 10% of background climatologic values. Eddies with smaller mixed layer depth anomalies, such as those in the summer and fall, have smaller vertical mixing flux anomalies that do not penetrate as deep into the water column (Figures 5a and 5b). Note that eddies with mixed layer depth anomalies in a direction opposite their expected isopycnal deformation (e.g., cyclones with anomalous deep mixed layer depths) are associated with smaller, less consistent, and less statistically significant vertical mixing flux anomalies (right half of Figure 5a). This is likely because these eddies are generally smaller, less well resolved and may not be actively mixing (Rohr et al., 2020).

Anomalies in the vertical distribution of biomass within South Pacific eddies are generally consistent with their associated mixed layer depth anomalies (Figures 5e and 5f). South Pacific cyclones with anomalously shallow mixed layer depths mix less biomass to depth (left half of Figure 5a), leading to an increase in surface biomass and decrease in biomass at depth relative to surrounding waters (left half of Figure 5e). The

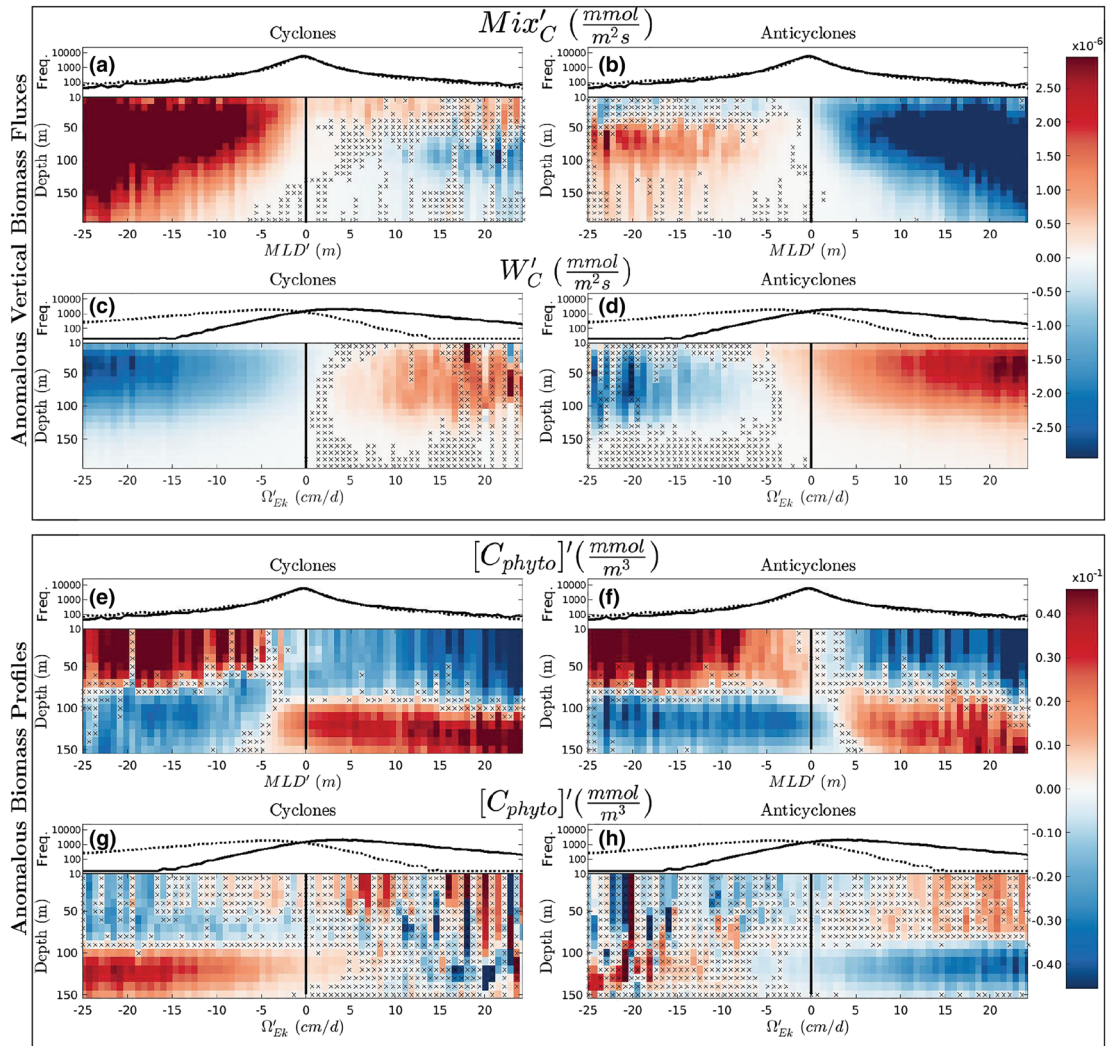


**Figure 5.** Anomalous biomass fluxes and concentrations associated with vertical transport mechanisms South Pacific eddies. Values are averaged across the same set of South Pacific eddies as in Figures 1, 2, 4, and 7. In the top half of the figure depth profiles are provided for the anomalous vertical (a, b) mixing flux of biomass ( $Mix'_C$ ) and (c, d) advection flux of biomass ( $W'_C$ ) in South Pacific cyclones (left) and anticyclones (right).  $Mix'_C$  and  $W'_C$  are plotted as a function of their driving mechanisms, the anomalous mixed layer depth ( $MLD'$ ), and the anomalous eddy-induced Ekman pumping velocity ( $\Omega'_{Ek}$ ), respectively. Fluxes are positive in the upward direction. In the bottom half of the figure, (e–h) depth profiles are provided for the anomalous biomass concentration associated with the same vertical transport mechanisms. Bins with anomalies that are statistically insignificant from 0 at the 95% confidence level are marked with a black x. The frequency of eddy realizations that fall in each bin on the x axis is plotted above the corresponding profiles; cyclonic (dashed lines) and anticyclonic (solid lines) distributions are included in each plot for comparison.

opposite is true in anticyclones with anomalous deep mixed layer depths (right half of Figures 5f and 5b). Modifications to the biomass profile in eddies with mixed layer depth anomalies in a direction opposite their expected isopycnal deformation (e.g., right half of Figures 5e) are associated with weak vertical mixing flux anomalies (e.g., right half of Figure 5a) and likely driven by eddy-induced Ekman pumping, which acts to advect biomass down in cyclones and up in anticyclones (see below).

### 3.3.4. Vertical Advection

Eddies with anomalous eddy-induced Ekman pumping velocities ( $\Omega'_{Ek}$ ) can physically advect biomass to different depths than surrounding waters via an anomalous vertical advection flux ( $W'_C$ ). Eddy-induced Ekman pumping velocities are necessarily anomalously downward in cyclones ( $-\Omega'_{Ek}$ ) and upward in anticyclones ( $+\Omega'_{Ek}$ ) due to the direction of the rotation of their surface currents (McGillicuddy, 2016). In turn, throughout the Southern Ocean the anomalous vertical advection flux is consistently downward ( $-W'_C$ ) in cyclones and upwards ( $+W'_C$ ) in anticyclones (Figures S14).

In the South Pacific, it is clear that almost all cyclones advect biomass down toward depth while anticyclones pump biomass up toward the surface relative to surrounding waters. There is little to no variability in the direction of anomalous eddy-induced Ekman pumping velocities within eddies of the same polarity (Figures 4g and 4h); however, the magnitude of these velocities generally increases to the south as the ambient wind speed over the ocean increases (Monahan, 2006). The magnitude and vertical penetration of the associated anomalous vertical advection flux increase with the magnitude of the anomalous eddy-induced Ekman pumping velocity (Figures 5c and 5d). Relative to background climatologic values, the magnitude of the vertical advection flux is actually slightly larger than that of the vertical mixing flux, even though the absolute magnitude is slightly lower. Note that the small subset of eddies associated with anomalous eddy-induced Ekman pumping velocities in a direction contradictory to their expected rotation (e.g.,  $+\Omega'_{\text{Ek}}$  in cyclones) are associated with smaller, less consistent, and less statistically significant vertical advection flux anomalies (e.g., right half of Figure 5c). This likely has to do with the misidentification of some other mesoscale features as eddies that may not be rotating as a coherent vortex.

Anomalies in the vertical distribution of biomass within South Pacific eddies are generally consistent with their associated vertical advection flux (Figures 5e and 5f). South Pacific cyclones with anomalously downward eddy-induced Ekman pumping velocities advect biomass to depth (left side of Figure 5c) leading to a decrease in surface biomass and increase in biomass at depth relative to surrounding waters (left side of Figure 5g). The opposite is true in anticyclones (right half of Figures 5d and 5h). Surface biomass anomalies are not as statistically significant, likely due to the competing effect of the anomalous vertical mixing flux which should affect the surface ocean more often than the deep ocean due to variability in the mixed layer depth. The small subset of eddies with anomalous eddy-induced Ekman pumping velocities in a direction contradictory to their expected rotation exhibit an inconsistent effect on the biomass profile (e.g., right half of Figure 5g), consistent with the likely misidentification of mesoscale features.

#### 3.4. Depth-Resolved Seasonal Variability

To better understand seasonal variability in the mechanisms by which eddies modify biomass across the water column, we examine the composite averaged annual cycle of depth-resolved anomaly profiles. Profiles of the anomalous carbon fluxes (Figures 6a–6d), biological rates (Figures 6e–6j), and biomass concentrations (Figures 6k and 6l) are averaged across all large eddies in the South Pacific ACC and plotted as a function of their seasonal progression. Throughout the year, diabatic mixing driven by mixed layer modification, and vertical advection, driven by eddy-induced Ekman pumping, transport biomass in competing directions (Figures 6a–6d). During the winter and spring, anomalous vertical transport is dominated by flux ( $Mix'_c$ ; Figures 6a and 6b), but during the summer and fall the magnitude of both mechanisms drops to similar levels. However, only the anomalous advection flux ( $W'_c$ ; Figures 6c and 6d) penetrates below the mixed layer where the magnitude of the anomalous mixing flux drops toward 0.

As biomass is vertically transported, it is simultaneously modified by biological mechanisms, which vary in strength and direction throughout the year. At any given depth and time, anomalous net population growth rates ( $r'$ ; Figures 6i and 6j) are driven by the difference between anomalous division rates ( $\mu'$ ; Figures 6e and 6f), which are driven by light and iron (see Rohr et al., 2020) and anomalous loss rates ( $l'$ ; Figures 6g and 6h), which are driven primarily by grazing (see section 3.2.2). In cyclones, local net population growth rates are depressed across the majority of the mixed layer throughout most of the year, particularly in the winter. The opposite is true in anticyclones. The magnitude of anomalous depth-averaged, biomass-weighted, net population growth rates is maximized when the *MLD* is shoaling in the early spring.

Depth-resolved biomass anomalies ( $[C'_{\text{phyto}}]$ ; Figures 6k and 6l) are in turn driven by contributions from both physical transport and biological mechanisms. In cyclones, biomass is elevated throughout the mixed layer during the winter when mixed layer depths are anomalously shallow (Figure 6k); even though biomass is reduced below the mixed layer relative to surrounding waters with deeper mixed layers, the net effect is an increase in depth-integrated biomass. In early spring the mixed layer begins to shoal, and the biomass anomaly flips direction, becoming anomalously low, both at the surface and integrated across the water column. By late spring biomass remains depressed in the upper ocean but becomes elevated at depth. This vertical gradient in the anomaly field remains through the summer and fall but decreases in magnitude as the year progresses. The net result is slightly depressed surface concentrations but slightly elevated depth-integrated inventories. The opposite is true in anticyclones (Figure 6l).

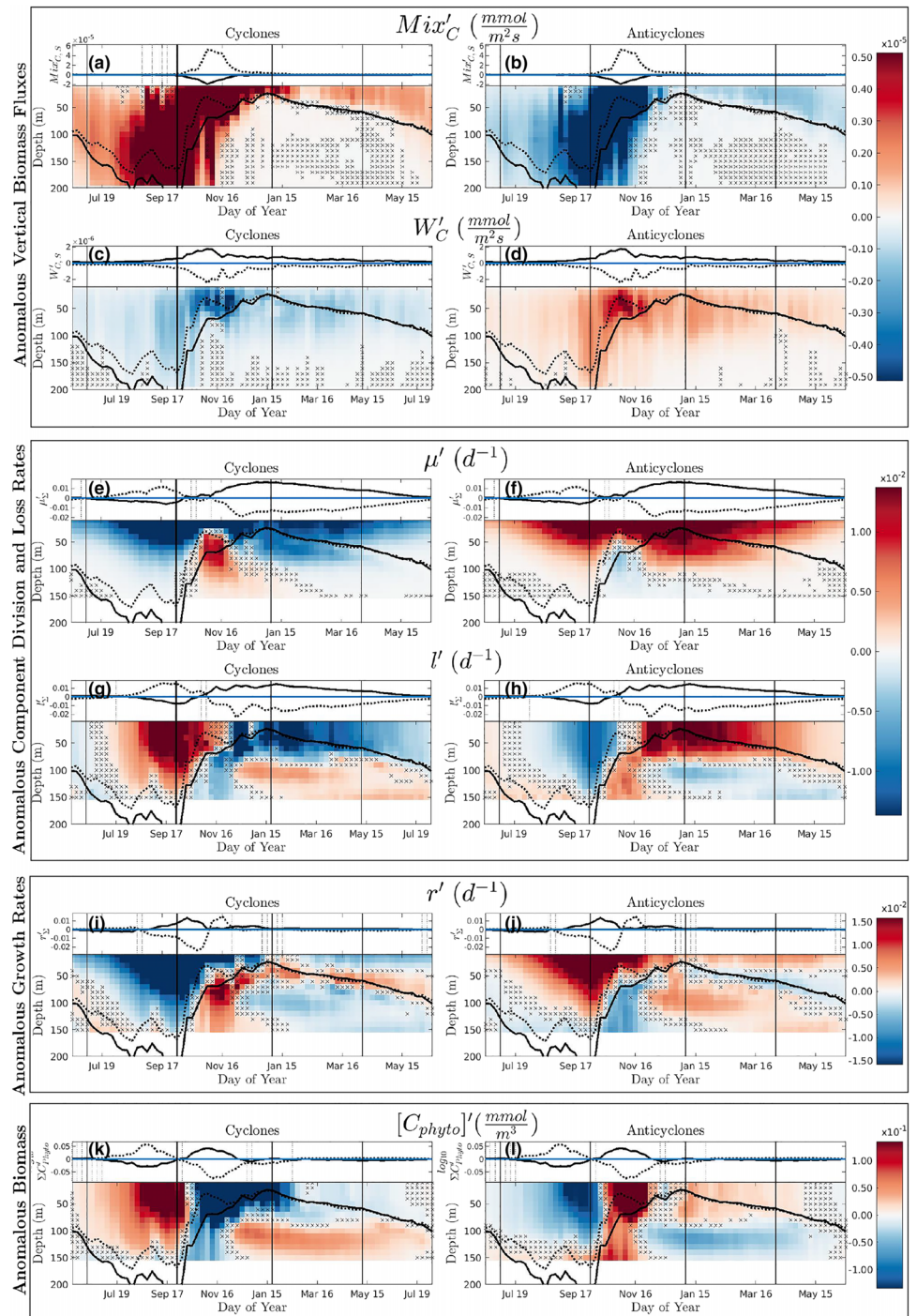


**Figure 6.** Composite averaged annual cycle of depth-resolved anomaly profiles in large South Pacific eddies within the ACC. Profiles of seasonal variability in  $Mix'_C$ ,  $W'_C$ ,  $\mu'_{\Sigma}$ ,  $l'_{\Sigma}$ ,  $r'_{\Sigma}$ , and  $[C_{phyto}]'$  are plotted for cyclones on the left and anticyclones on the right. The mean MLD in cyclones (dashed) and anticyclones (solid) is overlaid in black. Bins with anomalies that are statistically insignificant from 0 at the 95% confidence level are marked with a black x. Above each profile plot is either the corresponding (a–d) carbon flux into the surface ocean, (e–j) depth-averaged biomass-weighted mean, or (k, l) the depth-integrated biomass inventory. Cyclonic (dashed lines) and anticyclonic (solid lines) distributions are included in each plot for comparison. Bins in which the difference between cyclone and anticyclone anomalies is statistically insignificant at the 95% confidence level are marked with a dashed vertical line. Solid vertical lines delineate seasons.

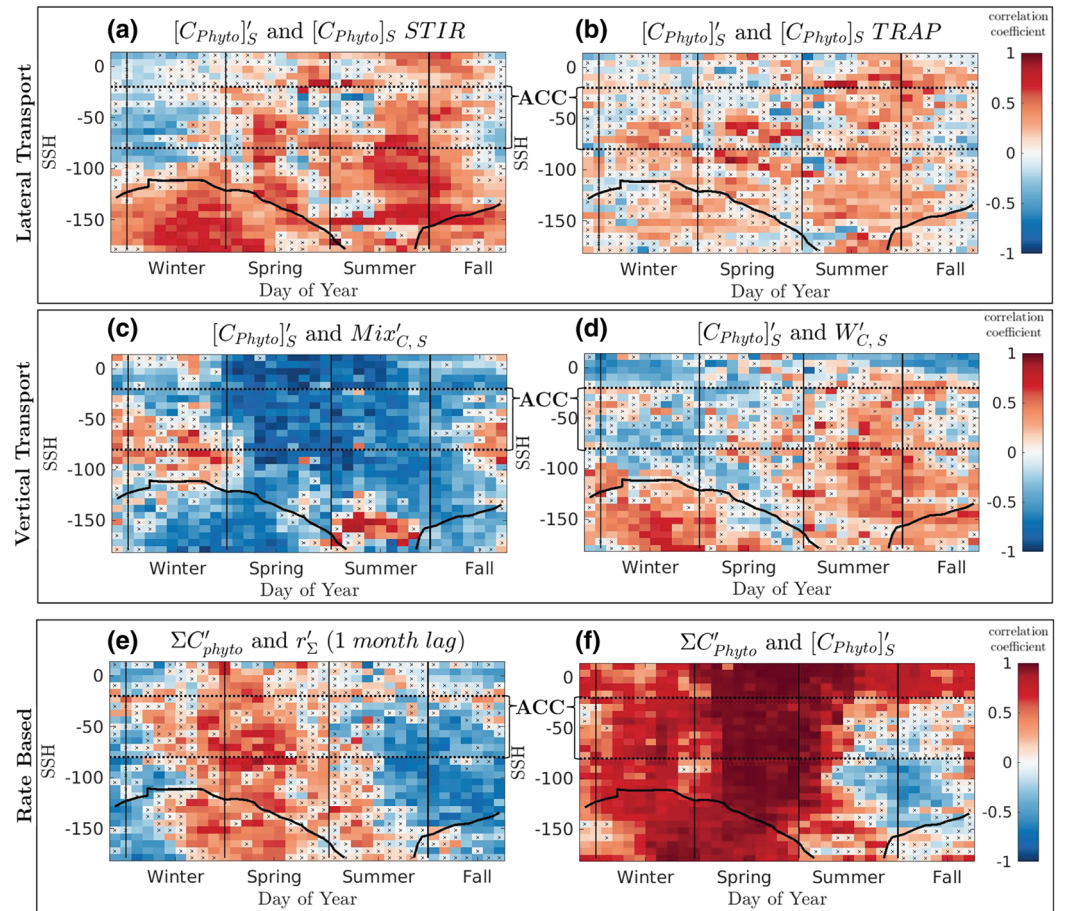


**Figure 7.** Spatial-temporal variability in the correlation between anomalous biomass and various variables associated with its drivers within South Pacific eddies. Type II correlation coefficients are computed independently for all eddies in a given spatial-temporal bin. The set of eddies in each bin is the same as Figures 1, 2, and 4; however, cyclones and anticyclones are not partitioned. Above, the simulated surface biomass anomaly ( $[C_{Phyto}]'_S$ ) is correlated with the potential for an anomaly to develop via lateral (a) stirring or (b) trapping. In the middle,  $[C_{Phyto}]'_S$  is correlated with the anomalous flux of carbon biomass into the surface via (c) diabatic mixing ( $Mix'_{C,S}$ ) and (d) advection ( $W'_{C,S}$ ). Below, the anomalous biomass inventory ( $\Sigma C'_{Phyto}$ ) is correlated with (e) the anomalous net population growth rate ( $r'_\Sigma$ ), which has been lagged by one month, and (f)  $[C_{Phyto}]'_S$ . The climatologic ice contour is overlaid in black. Bins with correlation coefficients that are statistically insignificant at the 95% confidence level are marked with a black x.

## 4. Discussion

### 4.1. Seasonal Variability in Mechanisms Driving Biomass Anomalies

Eddy-modified biomass anomalies are driven by a variety of different mechanisms at different times and in different places throughout the Southern Ocean. To help understand regional and seasonal variability in the causes of anomalous biomass it is useful to examine the correlation between anomalous biomass and the strength of its underlying drivers. Figure 7 provides distributions of the spatial-temporal variability of these correlations throughout the South Pacific. The set of eddies in each bin in Figure 7 is identical to Figures 1, 2, and 4, with the exception that cyclones and anticyclones are combined. By examining how the strength and direction in these correlations vary it is possible to infer when and where different mechanisms dominate what drives eddy-modified biomass anomalies. Seasonal variability in the mechanisms driving biomass anomalies in South Pacific ACC cyclones is described below and idealized in the schematic provided in Figure 8; similarly located anticyclones consistently respond in a symmetric manner.

#### 4.1.1. Deep Mixing Period from Late Fall Through Early Winter

During the late fall and early winter, anomalous biomass is predominantly driven by anomalous physical dilution. As the background mixed layer deepens, surface biomass concentrations are anomalously high in cyclones (Figure 1a) due to reduced physical dilution across anomalously shallow mixed layers (Figure 4e).

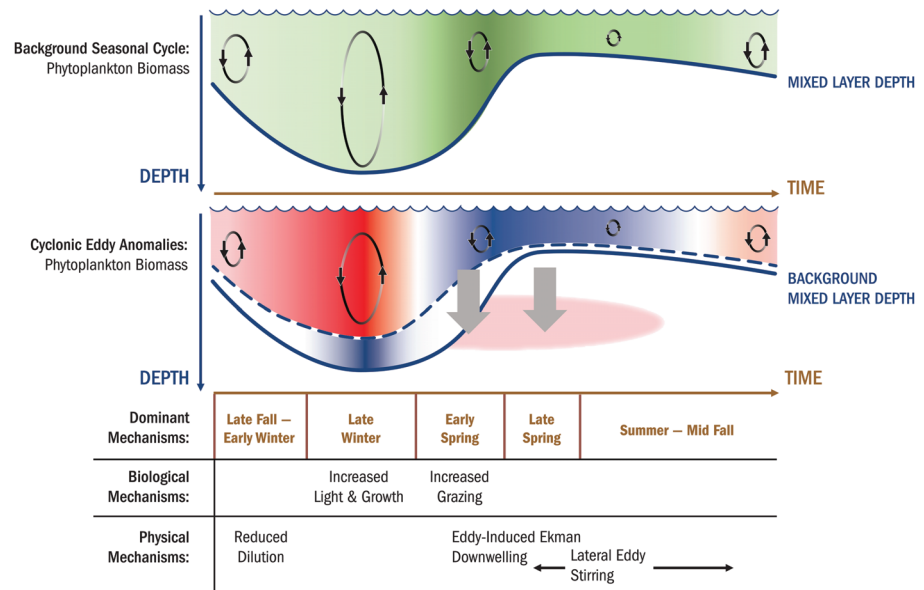


**Figure 8.** Schematic of dominant mechanisms driving anomalies in large South Pacific cyclones within the ACC. The idealized seasonal cycle for depth-resolved background and anomalous biomass is illustrated. Darker green indicates more background biomass, while red and blue indicate positive and negative anomalies, respectively. Circular and straight arrows indicate the vertical mixing and advection of biomass, respectively. Below, the seasonally variable dominant mechanisms driving these anomalies are denoted. The same mechanisms dominate in anticyclones, but induce anomalies in the opposite direction.

This is supported by the positive correlation between anomalous surface biomass and the anomalous mixing flux of biomass into the surface ocean (Figure 7c), indicating that surface concentrations increase ( $+ [C_{\text{Phyto}}]'_s$ ) as shallower mixed layer mix less biomass to depth ( $+ \text{Mix}'_{C,S}$ ). The strength of this correlation is stronger than that of anomalous surface biomass with any other plausible mechanism. Further, surface biomass increases disproportionately relative to depth-integrated biomass (Figures 1a and 1c), and the correlation between the two is weaker than in the spring (Figure 7f). This is consistent with biomass being consolidated across a shallower mixed layer depth relative to surrounding waters. Together, it appears that the initial reversal in the direction of observed surface chlorophyll anomalies in the South Pacific ACC (Dawson et al., 2018; Frenger et al., 2018; Song et al., 2018) is actually driven by physical dilution, not biological rates, at least while the mixed layer is still actively deepening. Moving forward, this is an important distinction, especially when inferring the depth-integrated response from surface chlorophyll observed from space.

#### 4.1.2. Late Winter Shoaling and the Spring Bloom

During the late winter and spring anomalous biomass is predominantly driven by eddy-modified biological rates and changes to new production. This is supported by a consistently strong, positive, and statistically significant correlation between depth-integrated biomass and net population growth rate anomalies from late winter until the end of spring (Figure 7e). The strength and consistency of this correlation is stronger than that of any other mechanism. For instance, the physical dilution of surface biomass is no longer relevant once mixed layer deepening ceases (Figure 7c) and lateral stirring is expected to induce anomalies in the wrong direction until midspring (Figures 4a and 7a Frenger et al., 2018). Although biomass anomalies are consistently driven by eddy-modified biological rates, the direction of biomass anomalies and the mechanisms that modify biological rates vary. During the late winter, both surface and depth-integrated biomass are elevated with annually maximized positive anomalies; however, during the spring both are depressed with annually minimized negative anomalies (Figures 1a and 1c). This flip in the sign of biomass anomalies is preceded by a flip in anomalous net population growth rates (Figure 2e), explaining why they remain positively correlated throughout the transition (Figure 7e).

During the late winter elevated biomass is preceded by elevated net population growth rates driven by elevated division rates. This is consistent with a bottom-up control and the hypothesis developed by Song et al. (2018) that elevated surface chlorophyll in spring ACC cyclones is driven by relieved light limitation.

Improved access to light in anomalously shallow mixed layers outweighs the suppressed vertical iron flux driven by eddy-induced Ekman downwelling. Moving into the spring, as the mixed layer shoals, depressed biomass is preceded by depressed net population growth rates driven by elevated loss rates. Even though division rates remain elevated through early spring, loss rates are elevated even more, indicative of a top-down control. Similar periods of top-down control associated with the shoaling of deep mixed layers have been observed in the North Atlantic (Behrenfeld et al., 2013) and simulated in the Southern Ocean (Rohr et al., 2017) and can be attributed to improved grazing efficiency when prey is more consolidated across a shallower mixed layer (Behrenfeld, 2010). Moving forward, it is important to remember that the largest simulated biomass anomalies in South Pacific ACC eddies are derived from changes to nutrient fluxes, light availability, and grazing pressure, as these processes can directly modify new production, the biological pump and larger-scale biogeochemical cycling.

#### 4.1.3. Quiescent Summer and Early Fall

During the quiescent summer and fall months anomalous surface biomass anomalies are predominantly driven by lateral stirring and vertical eddy-induced Ekman pumping. Depressed surface biomass concentrations, consistent with observations (Frenger et al., 2018), are generally positively correlated with the lateral stirring potential (Figure 7a). Note that the trapping potential is also often positively correlated with anomalous surface biomass; however, the stirring potential is generally larger, more consistently statistically significant, and better correlated with surface biomass anomalies than the trapping potential (Figures 4b and 4d; 7a and 7b). This is consistent with observations of stirring dominating trapping in the open ocean far from boundary currents with strong zonal chlorophyll gradients (Frenger et al., 2018). Depressed surface biomass is also positively correlated with the anomalous downward advection of biomass from the surface ocean (Figure 7d), which works to suppress surface biomass and inflate biomass at depth (Figures 5g and 6k).

Although surface biomass is anomalously low here, depth-integrated biomass is anomalously high due to the lingering effect of anomalous downward eddy-induced Ekman pumping during the spring bloom. The inflation of depth-integrated biomass can be explained by a strong anomalously downward advective flux of biomass out of densely populated surface waters during the spring, which can then persist below a shallow mixed layer throughout the summer and fall (Figure 6c). The lateral convergence of water needed to compensate for downwelling may also increase the depth-integrated biomass inventory. Moving forward, it is important to remember that surface biomass and depth-integrated biomass are not necessarily modified in the same direction.

#### 4.2. Basin-Scale Biomass Anomalies

Despite the pronounced spatiotemporal variability in simulated eddy-modified biomass anomalies, simulated cyclones and anticyclones consistently perturb biomass in opposite directions if they are in proximate regions at similar times. This symmetry leads to a large degree of averaging out at the basin scale. Although individual simulated eddies can exhibit anomalous biomass as high as 10–20% of background levels, particularly in the ACC, the rectified basin-scale effect is an order of magnitude smaller, consistent with observations (Frenger et al., 2018). The direction of the net simulated anomaly at the basin scale also varies by basin. For example, net anomalous depth-integrated biomass in cyclones is slightly negative in the South Pacific ACC but positive when integrated across the entire Southern Ocean. On average, in the simulated Southern Ocean at a given time there is a total of 743 t of anomalous depth-integrated carbon biomass in cyclones and –1,765 t in anticyclones. Together, that integrates out to an average –1,022 tonnes of anomalous biomass in all simulated Southern Ocean eddies at a given time. Qualitatively, observations agree that a negative net Southern Ocean anomaly in anticyclones dominates a net positive anomaly in cyclones leading to negative rectified basin-scale anomaly (Frenger et al., 2018).

Quantitatively, the magnitude of total spatially integrated anomalous biomass in all simulated Southern Ocean eddies is equal to roughly 0.5% of the corresponding background biomass, compared to 1–4% in the observations (Frenger et al., 2018). The larger magnitude in the observations can be attributed to a greater asymmetry in biomass anomalies between cyclones and anticyclones. The simulation likely does not represent this asymmetry as well due to its inability to represent the asymmetry in mixed layer depth anomalies (Rohr et al., 2020) that has been observed by Hausmann et al. (2017). If the magnitude of negative mixed layer depth anomalies in simulated cyclones was smaller, as observed, exacerbated light limitation could lead to decreased division rates and less biomass in simulated ACC cyclones during the late winter when anomalous division rates are driven by anomalous light availability (Rohr et al., 2020) and anomalous biomass is

driven by anomalous division rates. Less biomass in cyclones would increase the magnitude of the simulated asymmetry, in line with observations (Frenger et al., 2018). Note, though, that this simulation does not resolve sub mesoscale processes that could enhance the rectified iron supply (Brannigan, 2016; Mahadevan et al., 2008) and potentially increase net primary production in both cyclones and anticyclones.

Although the rectified basin-scale biomass anomaly appears relatively small, eddy-modified biomass anomalies, and variability in the source of these anomalies, could have a substantial effect on variability in  $CO_2$  gas exchange in the ACC, which is driven by a delicate balance between physical and biological processes in the Southern Ocean (Gottschalk et al., 2016) and remains one of the largest uncertainties in coupled climate models (Quére et al., 2007; Toggweiler & Russell, 2008). Gas exchange is likely particularly sensitive to eddy activity during the late winter and spring when anomalous biomass is largest and driven predominantly by modified light availability, nutrient fluxes and biological rates rather than physical transport. Even small modifications to bloom phenology, new production, biomass distributions, and export production in eddies could have important effects on the seasonal cycle of sea-air  $CO_2$  flux. Further, if eddy kinetic energy increases in the South Pacific as has been predicted (Patara et al., 2016), the net suppression of biomass in eddies could increase, reducing the size of the Southern Ocean  $CO_2$  sink (Mongwe et al., 2018) and damping its capacity to buffer to climate change.

### Acknowledgments

The CESM project is supported primarily by the National Science Foundation. This material is based upon work supported by the National Center for Atmospheric Research, which is a major facility sponsored by the National Science Foundation under Cooperative Agreement 1852977. Computing resources were provided by the Climate Simulation Laboratory at NCAR's Computational and Information Systems Laboratory (CISL). T. R. and S. C. D. acknowledge support from the National Aeronautics and Space Administration Ocean Biology and Biogeochemistry Program (NNX14AL86G) and the National Science Foundation Polar Programs Award 1440435 (Antarctic Integrated System Science) to the Palmer LTER program. P. G. acknowledges support from the National Aeronautics and Space Administration Physical Oceanography program (NNX16AH9G) and the National Science Foundation Award OCE-1558809. Thank you to Hajoon Song and Ivy Frenger for their work that inspired and supported this analysis. Complete observational eddy tracks are available online (<http://wombat.coas.oregonstate.edu/eddies/index.html>). The code used to track eddies in the model domain can be found at <https://github.com/jfaghm/OceanEddies> with detailed information publicly available on data: DOI: 10.1038/sdata.2015.28. Complete simulated eddy tracks, along with the complete catalogue of environmental variables and anomalies within these eddies, are available in a .mat data structure at [osf.io/cw7qt](https://osf.io/cw7qt), DOI 10.17605/OSF.IO/CW7QT. The primary scripts used to filter, plot, and analyze this data, in addition to extensive metadata information, can also be found at [osf.io/cw7qt](https://osf.io/cw7qt), DOI 10.17605/OSF.IO/CW7QT.

### 5. Conclusions

Simulated Southern Ocean eddies can modify phytoplankton via several distinct pathways, leading to a large degree of regional and seasonal variability in the ensuing biomass anomalies within them. From a biological perspective, biomass is typically subject to depressed net population growth rates in cyclones driven from the bottom-up by depressed division rates. The opposite is true in anticyclones. From a physical perspective, lateral transport is dominated by stirring rather than trapping throughout the year. Vertical transport is controlled by both diabatic mixing across anomalous mixed layer depths and advection via eddy-induced Ekman pumping. However, the relative dominance of these mechanisms is subject to regional and seasonal variability, driven by ambient environmental conditions. The most dramatic and coherent seasonal cycle is in the South Pacific ACC. Here, in cyclones, both surface and depth-integrated biomass is elevated in the winter and depressed in the summer. During the summer and fall surface biomass is depressed but depth-integrated biomass is enhanced. The opposite is true anticyclones. In all South Pacific ACC eddies, anomalous biomass is primarily driven by physical dilution via vertical mixing in the late fall and early winter, biological mechanisms in the late winter and spring, and stirring and eddy-induced Ekman pumping in the summer and early fall. The largest biomass anomalies exceed 20% of background levels and occur during the spring bloom period, when eddies induce biomass anomalies by stimulating or suppressing new production, rather than physically transporting existing biomass. Even local eddy mediated changes to new production likely have important implications for the biological pump, and sea-air  $CO_2$  flux. Spatiotemporal variability, in conjunction with the largely symmetric response to cyclones and anticyclones, leads to basin-scale biomass anomalies that are an order of magnitude smaller than those in individual eddies. Nevertheless, a small asymmetry does exist at the basin scale: on average, net depressed biomass in cyclones dominates net enhanced biomass in anticyclones, leading to a net depression of biomass when integrated across the Southern Ocean throughout the year. Moving forward, much care will be needed when scaling up local observations or inferring their implications on larger biogeochemical cycling, as eddy-modified anomalies can derive from fundamentally different mechanisms at different times and in different places.

### References

- Behrenfeld, M. J. (2010). Abandoning Sverdrup's Critical Depth Hypothesis on phytoplankton blooms. *Ecology*, *91*(4), 977–989. <https://doi.org/10.1890/09-1207.1>
- Behrenfeld, M. J., Doney, S. C., Lima, I. D., Boss, E. S., & Siegel, D. A. (2013). Annual cycles of ecological disturbance and recovery underlying the subarctic Atlantic spring plankton bloom. <https://doi.org/10.1002/gbc.20050>
- Beron-Vera, F. J., Wang, Y., Olascoaga, M. J., Goni, G. J., & Haller, G. (2013). Objective detection of oceanic eddies and the Agulhas Leakage. *Journal of Physical Oceanography*, *43*(7), 1426–1438. <https://doi.org/10.1175/JPO-D-12-0171.1>
- Boyd, P. W. (2002). Environmental factors controlling phytoplankton processes in the Southern Ocean. *Journal of Phycology*, *38*(5), 844–861. <https://doi.org/10.1046/j.1529-8817.2002.t01-1-01203.x>
- Boyd, P. W., Crossley, A. C., DiTullio, G. R., Griffiths, F. B., Hutchins, D. A., Queguiner, B., et al. (2001). Control of phytoplankton growth by iron supply and irradiance in the subantarctic Southern Ocean: Experimental results from the SAZ Project. *Journal of Geophysical Research*, *106*(C12), 31,573–31,583. <https://doi.org/10.1029/2000JC000348>
- Brannigan, L. (2016). Intense submesoscale upwelling in anticyclonic eddies. *Geophysical Research Letters*, *43*, 3360–3369. <https://doi.org/10.1002/2016GL067926>

- Carranza, M. M., & Gille, S. T. (2015). Southern Ocean wind-driven entrainment enhances satellite chlorophyll-a through the summer. *Journal of Geophysical Research: Oceans*, *120*, 304–323. <https://doi.org/10.1002/2014JC010203>
- Carranza, M. M., Gille, S. T., Franks, P. J. S., Johnson, K. S., Pinkel, R., & Girtton, J. B. (2018). When mixed layers are not mixed. Storm-driven mixing and bio-optical vertical gradients in mixed layers of the Southern Ocean. *Journal of Geophysical Research: Oceans*, *123*, 7264–7289. <https://doi.org/10.1029/2018JC014416>
- Chelton, D. B., Gaube, P., Schlax, M. G., Early, J. J., & Samelson, R. M. (2011). The influence of nonlinear mesoscale eddies on near-surface oceanic chlorophyll. *Science (New York, N.Y.)*, *334*(6054), 328–332. <https://doi.org/10.1126/science.1208897>
- Chelton, D. B., Schlax, M. G., & Samelson, R. M. (2011). Global observations of nonlinear mesoscale eddies. *Progress in Oceanography*, *91*(2), 167–216. <https://doi.org/10.1016/j.pocean.2011.01.002>
- Dawson, H. R. S., Strutton, P. G., & Gaube, P. (2018). The unusual surface chlorophyll signatures of Southern Ocean eddies. *Journal of Geophysical Research: Oceans*, *123*, 6053–6069. <https://doi.org/10.1029/2017JC013628>
- Deppeler, S. L., & Davidson, A. T. (2017). Southern Ocean Phytoplankton in a Changing Climate. *Frontiers in Marine Science*, *4*(40), 1–28. <https://doi.org/10.3389/fmars.2017.00040>
- Dewar, W. K., & Flierl, G. R. (1987). Some effects of the wind on rings. *Journal of Physical Oceanography*, *17*(10), 1653–1667. [https://doi.org/10.1175/1520-0485\(1987\)017<1653:SEOTWOi2.0.CO;2](https://doi.org/10.1175/1520-0485(1987)017<1653:SEOTWOi2.0.CO;2)
- Doney, S. C., Glover, D. M., McCue, S. J., & Fuentes, M. (2003). Mesoscale variability of Sea-viewing Wide Field-of-view Sensor (SeaWiFS) satellite ocean color: Global patterns and spatial scales. *Journal of Geophysical Research*, *108*(C2), 3024. <https://doi.org/10.1029/2001JC000843>
- Doney, S. C., Lima, I., Moore, J. K., Lindsay, K., Behrenfeld, M. J., Westberry, T. K., et al. (2009). Skill metrics for confronting global upper ocean ecosystem-biogeochemistry models against field and remote sensing data. *Journal of Marine Systems*, *76*(1), 95–112. <https://doi.org/10.1016/j.jmarsys.2008.05.015>
- Dufois, F., Hardman-Mountford, N. J., Greenwood, J., Richardson, A. J., Feng, M., Herbette, S., & Matear, R. (2014). Impact of eddies on surface chlorophyll in the South Indian Ocean. *Journal of Geophysical Research: Oceans*, *119*, 8061–8077. <https://doi.org/10.1002/2014JC010164>
- Dufois, F., Hardman-Mountford, N. J., Greenwood, J., Richardson, A. J., Feng, M., & Matear, R. J. (2016). Anticyclonic eddies are more productive than cyclonic eddies in subtropical gyres because of winter mixing. *Science Advances*, *2*(5), e1600282. <https://doi.org/10.1126/sciadv.1600282>
- Early, J. J., Samelson, R. M., & Chelton, D. B. (2011). The evolution and propagation of quasigeostrophic ocean eddies. *Journal of Physical Oceanography*, *41*(8), 1535–1555. <https://doi.org/10.1175/2011JPO4601.1>
- Faghmous, J. H., Frenger, I., Yao, Y., Warmka, R., Lindell, A., & Kumar, V. (2015). A daily global mesoscale ocean eddy dataset from satellite altimetry. *Scientific Data*, *2*. <https://doi.org/10.1038/sdata.2015.28>
- Falkowski, P. G., Ziemann, D., Kolber, Z., & Bienfang, P. K. (1991). Role of eddy pumping in enhancing primary production in the ocean. *Nature*, *352*(6330), 55. <https://doi.org/10.1038/352055a0>
- Fauchereau, N., Tagliabue, A., Bopp, L., & Monteiro, P. M. S. (2011). The response of phytoplankton biomass to transient mixing events in the Southern Ocean. *Geophysical Research Letters*, *38*, L17601. <https://doi.org/10.1029/2011GL048498>
- Fiksen, Ø. (2000). The adaptive timing of diapause—A search for evolutionarily robust strategies in *Calanus finmarchicus*. *ICES Journal of Marine Science*, *57*(6), 1825–1833. <https://doi.org/10.1006/jmsc.2000.0976>
- Flierl, G. R. (1981). Particle motions in large-amplitude wave fields. *Geophysical & Astrophysical Fluid Dynamics*, *18*(1-2), 39–74. <https://doi.org/10.1080/03091928108208773>
- Frenger, I., Münnich, M., & Gruber, N. (2018). Imprint of Southern Ocean eddies on chlorophyll. *Biogeosciences Discussions*, 1–26. <https://doi.org/10.1080/03091928108208773>
- Frenger, I., Münnich, M., Gruber, N., & Knutti, R. (2015). Southern Ocean eddy phenomenology. *Journal of Geophysical Research: Oceans*, *120*, 7413–7449. <https://doi.org/10.1002/2015JC011047>
- Gaube, P., Chelton, D. B., Samelson, R. M., Schlax, M. G., & O'Neill, L. W. (2015). Satellite observations of mesoscale eddy-induced Ekman pumping. <https://doi.org/10.1175/JPO-D-14-0032.1>
- Gaube, P., & McGillicuddy, D. J. (2017). The influence of Gulf Stream eddies and meanders on near-surface chlorophyll. *Deep Sea Research Part I: Oceanographic Research Papers*, *122*, 1–16. <https://doi.org/10.1016/j.dsr.2017.02.006>
- Gaube, P., McGillicuddy, D. J., & Moulin, A. J. (2019). Mesoscale eddies modulate mixed layer depth globally. *Geophysical Research Letters*, *46*, 1505–1512. <https://doi.org/10.1029/2018GL080006>
- Gaube, P., McGillicuddy, D., Chelton, D. B., Behrenfeld, M. J., & Strutton, P. G. (2014). Regional variations in the influence of mesoscale eddies on near-surface chlorophyll. *Journal of Geophysical Research: Oceans*, *119*, 8195–8220. <https://doi.org/10.1002/2014JC010111>
- Glover, D. M., Doney, S. C., Oestreich, W. K., & Tullo, A. W. (2018). Geostatistical analysis of mesoscale spatial variability and error in SeaWiFS and MODIS/ Aqua global ocean color data. *Journal of Geophysical Research: Oceans*, *123*, 22–39. <https://doi.org/10.1002/2017JC013023>
- Gottschalk, J., Skinner, L. C., Lippold, J., Vogel, H., Frank, N., Jaccard, S. L., & Waelbroeck, C. (2016). Biological and physical controls in the Southern Ocean on past millennial-scale atmospheric CO<sub>2</sub> changes. *Nature Communications*, *7*(1), 1–11. <https://doi.org/10.1038/ncomms11539>
- Griffies, S., Biastoch, A., Boning, C., Bryan, F., Danabasoglu, G., Chassignet, E., et al. (2009). Coordinated Ocean-ice Reference Experiments (CORES). *Ocean Modelling*, *26*(1-2), 1–46. <https://doi.org/10.1016/j.ocemod.2008.08.007>
- Haller, G. (2015). Lagrangian coherent structures. *Annual Review of Fluid Mechanics*, *47*(1), 137–162. <https://doi.org/10.1146/annurev-fluid-010313-141322>
- Harrison, C. S., Long, M. C., Lovenduski, N. S., & Moore, J. K. (2018). Mesoscale effects on carbon export: A global perspective. *Global Biogeochemical Cycles*, *32*, 680–703. <https://doi.org/10.1002/2017GB005751>
- Hauck, J., Völker, C., Wolf-Gladrow, D. A., Laufkötter, C., Vogt, M., Aumont, O., et al. (2015). On the Southern Ocean CO<sub>2</sub> uptake and the role of the biological carbon pump in the 21st century. *Global Biogeochemical Cycles*, *29*, 1451–1470. <https://doi.org/10.1002/2015GB005140>
- Hausmann, U., McGillicuddy, D. J., & Marshall, J. (2017). Observed mesoscale eddy signatures in Southern Ocean surface mixed-layer depth. *Journal of Geophysical Research: Oceans*, *122*, 617–635. <https://doi.org/10.1002/2016JC012225>
- Holling, C. S. (1959). Some characteristics of simple types of predation and parasitism. *The Canadian Entomologist*, *91*(7), 385–398. <https://doi.org/10.4039/Ent91385-7>
- Hunke, E. C., & Lipscomb, W. H. (2008). CICE: The Los Alamos Sea Ice Model. Documentation and software user's manual. Version 4.0. Los Alamos National Laboratory, Tech. Rep. LA-CC-06-012.

- Large, W. G. (1998). Modeling and parameterizing the ocean planetary boundary layer. *Ocean modeling and parameterization* pp. 81–120). NATO Science Series. Dordrecht: Springer. <https://doi.org/10.1007/978-94-011-5096-53>
- Large, W. G., McWilliams, J. C., & Doney, S. C. (1994). Oceanic vertical mixing: A review and a model with a nonlocal boundary layer parameterization. *Reviews of Geophysics*, 32(4), 363–403. <https://doi.org/10.1029/94RG01872>
- Large, W. G., & Yeager, S. (2004). Diurnal to decadal global forcing for ocean and sea-ice models: The data sets and flux climatologies. <https://doi.org/10.5065/D6KK98Q6>
- Laufkötter, C., Vogt, M., Gruber, N., Aita-Noguchi, M., Aumont, O., Bopp, L., et al. (2015). Drivers and uncertainties of future global marine primary production in marine ecosystem models. *Biogeosciences*, 12(23), 6955–6984. <https://doi.org/10.5194/bg-12-6955-2015>
- Le Quéré, C., Buitenhuis, E. T., Moriarty, R., Alvain, S., Aumont, O., Bopp, L., et al. (2016). Role of zooplankton dynamics for Southern Ocean phytoplankton biomass and global biogeochemical cycles. *Biogeosciences*, 13(14), 4111–4133. <https://doi.org/10.5194/bg-13-4111-2016>
- Lehahn, Y., d'Ovidio, F., Lévy, M., Amitai, Y., & Heifetz, E. (2011). Long range transport of a quasi isolated chlorophyll patch by an Agulhas ring. *Geophysical Research Letters*, 38, L16610. <https://doi.org/10.1029/2011GL048588>
- Lima, I. D., Lam, P. J., & Doney, S. C. (2014). Dynamics of particulate organic carbon flux in a global ocean model. *Biogeosciences*, 11(4), 1177–1198. <https://doi.org/10.5194/bg-11-1177-2014>
- Long, M. C., Lindsay, K., Peacock, S., Moore, J. K., & Doney, S. C. (2013). Twentieth-century oceanic carbon uptake and storage in CESM1 (BGC). *Journal of Climate*, 26(18), 6775–6800. <https://doi.org/10.1175/JCLI-D-12-00184.1>
- Mahadevan, A., Thomas, L. N., & Tandon, A. (2008). Comment on “Eddy/wind interactions stimulate extraordinary mid-ocean plankton blooms”. *Science (New York, N.Y.)*, 320(5875), 448–448. <https://doi.org/10.1126/science.1152111>
- Marinov, I., Gnanadesikan, A., Sarmiento, J. L., Toggweiler, J. R., Follows, M. J., & Mignone, B. K. (2008). Impact of oceanic circulation on biological carbon storage in the ocean and atmospheric pCO<sub>2</sub>. <https://doi.org/10.1029/2007GB002958>
- McGillicuddy, D. J. (2016). Mechanisms of physical-biological-biogeochemical interaction at the oceanic mesoscale. *Annual Review of Marine Science*, 8(1), 125–159. <https://doi.org/10.1146/annurev-marine-010814-015606>
- McGillicuddy, D. J., Anderson, L. A., Bates, N. R., Bibby, T., Buesseler, K. O., Carlson, C. A., et al. (2007). Eddy/wind interactions stimulate extraordinary mid-ocean plankton blooms. *Science (New York, N.Y.)*, 316(5827), 1021–1026. <https://doi.org/10.1126/science.1136256>
- Meredith, M. P. (2016). Understanding the structure of changes in the Southern Ocean eddy field. *Geophysical Research Letters*, 43, 5829–5832. <https://doi.org/10.1002/2016GL069677>
- Monahan, A. H. (2006). The probability distribution of sea surface wind speeds. Part I: Theory and SeaWinds observations. *Journal of Climate*, 19(4), 497–520. <https://doi.org/10.1175/JCLI3640.1>
- Mongwe, N. P., Vichi, M., & Monteiro, P. M. S. (2018). The seasonal cycle of pCO<sub>2</sub> and CO<sub>2</sub> fluxes in the Southern Ocean: Diagnosing anomalies in CMIP5 Earth system models. *Biogeosciences*, 15(9), 2851–2872. <https://doi.org/10.5194/bg-15-2851-2018>
- Moore, J. K., & Braucher, O. (2008). Sedimentary and mineral dust sources of dissolved iron to the world ocean. *Biogeosciences*, 5(3), 631–656. <https://doi.org/10.5194/bg-5-631-2008>
- Moore, J. K., Doney, S. C., & Lindsay, K. (2004). Upper ocean ecosystem dynamics and iron cycling in a global three-dimensional model. *Global Biogeochemical Cycles*, 18, GB4028. <https://doi.org/10.1029/2004GB002220>
- Moore, J. K., Lindsay, K., Doney, S. C., Long, M. C., & Misumi, K. (2013). Marine ecosystem dynamics and biogeochemical cycling in the Community Earth System Model [CESM1(BGC)]: Comparison of the 1990s with the 2090s under the RCP4.5 and RCP8.5 Scenarios. *Journal of Climate*, 26(23), 9291–9312.
- Morrison, A. K., Frölicher, T. L., & Sarmiento, J. L. (2014). Upwelling in the Southern Ocean. *Physics Today*, 68(1), 27–32. <https://doi.org/10.1175/JCLI-D-12-00566.1>
- Nelson, D. M., & Smith, W. O. (1991). Sverdrup revisited: Critical depths, maximum chlorophyll levels, and the control of Southern Ocean productivity by the irradiance-mixing regime. *Limnology and Oceanography*, 36(8), 1650–1661. <https://doi.org/10.4319/lo.1991.36.8.1650>
- Patara, L., Böning, C. W., & Biastoch, A. (2016). Variability and trends in Southern Ocean eddy activity in 1/12° ocean model simulations. *Geophysical Research Letters*, 43, 4517–4523. <https://doi.org/10.1002/2016GL069026>
- Quéré, C. L., Rödenbeck, C., Buitenhuis, E. T., Conway, T. J., Langenfelds, R., Gomez, A., et al. (2007). Saturation of the Southern Ocean CO<sub>2</sub> sink due to recent climate change. *Science*, 316(5832), 1735–1738. <https://doi.org/10.1126/science.1136188>
- Rohr, T., Harrison, C., Long, M. C., Gaube, P., & Doney, S. C. (2020). Eddy-modified iron, light, and phytoplankton cell division rates in the simulated Southern Ocean. *Global Biogeochemical Cycles*, 34, e2019GB006380. <https://doi.org/10.1029/2019GB006380>
- Rohr, T., Long, M., Kavanaugh, M. T., Lindsay, K., & Doney, S. (2017). Variability in the mechanisms controlling Southern Ocean phytoplankton bloom phenology in an ocean model and satellite observations. *Global Biogeochemical Cycles*, 31, 922–940. <https://doi.org/10.1002/2016GB005615>
- Sailley, S., Vogt, M., Doney, S., Aita, M. N., Bopp, L., Buitenhuis, E., et al. (2013). Comparing food web structures and dynamics across a suite of global marine ecosystem models. *Ecological Modelling*, 261–262, 43–57. <https://doi.org/10.1016/j.ecolmodel.2013.04.006>
- Sakshaug, E., & Holm-Hansen, O. (1986). Photoadaptation in Antarctic phytoplankton: Variations in growth rate, chemical composition and P versus I curves. *Journal of Plankton Research*, 8(3), 459–473. <https://doi.org/10.1093/plankt/8.3.459>
- Siegel, D. A., Buesseler, K. O., Doney, S. C., Sailley, S. F., Behrenfeld, M. J., & Boyd, P. W. (2014). Global assessment of ocean carbon export by combining satellite observations and food-web models. *Global Biogeochemical Cycles*, 28, 181–196. <https://doi.org/10.1002/2013GB004743>
- Siegel, D. A., McGillicuddy, D. J., & Fields, E. A. (1999). Mesoscale eddies, satellite altimetry, and new production in the Sargasso Sea. *Journal of Geophysical Research*, 104, 13,359–13,379. <https://doi.org/10.1029/1999JC900051>
- Smetacek, V., Assmy, P., & Henjes, J. (2004). The role of grazing in structuring Southern Ocean pelagic ecosystems and biogeochemical cycles. *Antarctic Science*, 16(4), 541–558. <https://doi.org/10.1017/S0954102004002317>
- Smith, R., Jones, P., Briegleb, P., Bryan, O., Danabasoglu, G., Dennis, M., et al. (2010). The Parallel Ocean Program (POP) reference manual: Ocean component of the Community Climate System Model (CCSM).
- Smith, W. O., Nelson, D. M., & Mathot, S. (1999). Phytoplankton growth rates in the Ross Sea, Antarctica, determined by independent methods: Temporal variations. *Journal of Plankton Research*, 21(8), 1519–1536. <https://doi.org/10.1093/plankt/21.8.1519>
- Song, H., Long, M. C., Gaube, P., Frenger, I., Marshall, J., & McGillicuddy, D. J. (2018). Seasonal variation in the correlation between anomalies of sea level and chlorophyll in the Antarctic Circumpolar Current. *Geophysical Research Letters*, 45, 5011–5019. <https://doi.org/10.1029/2017GL076246>
- Spies, A. (1987). Growth rates of Antarctic marine phytoplankton in the Weddell Sea. *Marine Ecology Progress Series*, 41(3), 267–274.
- Tamsitt, V., Drake, H. F., Morrison, A. K., Talley, L. D., Dufour, C. O., Gray, A. R., et al. (2017). Spiraling pathways of global deep waters to the surface of the Southern Ocean. *Nature Communications*, 8(1), 172. <https://doi.org/10.1038/s41467-017-00197-0>

- Toggweiler, J. R., & Russell, J. (2008). Ocean circulation in a warming climate. *Nature*, *451*(7176), 286–288. <https://doi.org/10.1038/nature06590>
- Uitz, J., Claustre, H., Morel, A., & Hooker, S. B. (2006). Vertical distribution of phytoplankton communities in open ocean: An assessment based on surface chlorophyll. *Journal of Geophysical Research*, *111*, C08005. <https://doi.org/10.1029/2005JC003207>
- Varpe, Ø. (2012). Fitness and phenology: Annual routines and zooplankton adaptations to seasonal cycles. *Journal of Plankton Research*, *34*(4), 267–276. <https://doi.org/10.1093/plankt/fbr108>